# Panchromatic SED modelling of spatially resolved galaxies

## Daniel J. B. Smith[1]* and Christopher C. Hayward[2,3]

[1]*Centre for Astrophysics, Science & Technology Research Institute, University of Hertfordshire, Hatfield, Herts, AL10 9AB, UK*
[2]*Center for Computational Astrophysics, Flatiron Institute, 162 Fifth Avenue, New York, NY 10010, USA*
[3]*Harvard–Smithsonian Center for Astrophysics, 60 Garden Street, Cambridge, MA 02138, USA*

## ABSTRACT

We test the efficacy of the energy-balance spectral energy distribution (SED) fitting code MAGPHYS for recovering the spatially resolved properties of a simulated isolated disc galaxy, for which it was not designed. We perform 226 950 MAGPHYS SED fits to regions between 0.2 and 25 kpc in size across the galaxy's disc, viewed from three different sight-lines, to probe how well MAGPHYS can recover key galaxy properties based on 21 bands of UV–far-infrared model photometry. MAGPHYS yields statistically acceptable fits to >99 per cent of the pixels within the *r*-band effective radius and between 59 and 77 percent of pixels within 20 kpc of the nucleus. MAGPHYS is able to recover the distribution of stellar mass, star formation rate (SFR), specific SFR, dust luminosity, dust mass, and *V*-band attenuation reasonably well, especially when the pixel size is $\gtrsim 1$ kpc, whereas non-standard outputs (stellar metallicity and mass-weighted age) are recovered less well. Accurate recovery is more challenging in the smallest sub-regions of the disc (pixel scale $\lesssim 1$ kpc), where the energy balance criterion becomes increasingly incorrect. Estimating integrated galaxy properties by summing the recovered pixel values, the true integrated values of all parameters considered except metallicity and age are well recovered at all spatial resolutions, ranging from 0.2 kpc to integrating across the disc, albeit with some evidence for resolution-dependent biases. These results must be considered when attempting to analyse the structure of real galaxies with actual observational data, for which the 'ground truth' is unknown.

**Key words:** radiative transfer – dust, extinction – galaxies: fundamental parameters – galaxies: ISM – galaxies: stellar content – infrared: galaxies.

## 1 INTRODUCTION

Contemporary observational astrophysics is extremely data rich; we have never had a larger range of survey data, covering wavelengths ranging from the ultraviolet to the far-infrared and sub-millimetre. Whatever the wavelength, the data have never been more sensitive, or sharper, whether obtained from the ground (e.g. Hartley et al. 2013; Jarvis et al. 2013; Tanaka et al. 2017), using interferometers (such as LOFAR: Hardcastle et al. 2016, or ALMA: Dunlop et al. 2017) or from space (e.g. with *Herschel*: Kennicutt et al. 2011, or the *Hubble Space Telescope*: Illingworth et al. 2013). This means that we are becoming able to go beyond modelling the integrated multiwavelength emission from galaxies, and beyond modelling individual components (performing bulge/disc decomposition, e.g. Vika et al. 2014; Kennedy et al. 2016; Johnston et al. 2017), to modelling individual pixels at all wavelengths simultaneously, building up unprecedented understanding of the physics of

galaxy formation and evolution. One of the many benefits of this is that the widely used panchromatic modelling techniques such as MAGPHYS (da Cunha, Charlot & Elbaz 2008) and CIGALE (Burgarella, Buat & Iglesias-Páramo 2005; Noll et al. 2009) use energetic arguments to build a consistent model of all these data simultaneously, bringing the starlight that dominates the luminosity at optical/near-infrared wavelengths on to an even footing with the dust emission that dominates at mid- and far-infrared wavelengths. In the real Universe, this is complicated by the potentially very different resolutions afforded by observations at different wavelengths (e.g. optical versus far-infrared data), though techniques exist to deconvolve the data and perhaps prevent observational effects from biasing the results (see e.g. Viero et al. 2013; Merlin et al. 2015; Wright et al. 2016; Hurley et al. 2017).

The aforementioned MAGPHYS code uses a physically motivated model to consistently model the multiwavelength properties of galaxies from the rest-frame ultraviolet to the far-infrared. By balancing the energy absorbed by dust at optical/near-infrared wavelengths with the far-infrared luminosity, consistently modelling the emission from the stars and dust simultaneously can give a greater

* E-mail: d.j.b.smith@herts.ac.uk

degree of understanding than considering either wavelength range alone (e.g. Smith et al. 2012), since around half of the photons ever emitted by stars and AGN have been absorbed and re-radiated by dust (e.g. Dole et al. 2006). Only by studying all of the available data simultaneously can we hope to build up a full picture of the mass growth through star formation in galaxies, their dust mass evolution, and the role of environment, for example. As a result, MAGPHYS has been widely used throughout the literature (e.g. da Cunha et al. 2010; Smith et al. 2012; Berta et al. 2013; Lanz et al. 2013; Rowlands et al. 2014a,b; Viaene et al. 2014; Hayward & Smith 2015; Smith & Hayward 2015; Dariush et al. 2016; Viaene et al. 2016; Miettinen et al. 2017; Gurkan et al. 2018), and the same is true of CIGALE (e.g. Giovannoli et al. 2011; Johnston et al. 2015; Wylezalek et al. 2016; Pearson et al. 2017). One key advantage of MAGPHYS over other SED fitting codes is that the required SED libraries are pre-defined and publicly available, which means that results produced by different groups are directly comparable since they use the same priors, stellar population library, star formation histories, and dust law. This ensures that the results obtained by any group are repeatable given the same input photometry.

Particular among the MAGPHYS investigations, Hayward & Smith (2015) performed an idealized test of the extent to which MAGPHYS is able to recover reliable properties of galaxies by analysing a suite of smoothed-particle-hydrodynamical (SPH) simulations on which dust radiative transfer was performed in post-processing to compute UV–mm spectral energy distributions (SEDs) of the simulated galaxies. The advantages of testing MAGPHYS in this way are wide-ranging: since the true properties (e.g. stellar mass, star formation rate, etc.) of the galaxies being modelled are known, and since we can eliminate uncertainties due to e.g. the uncertainty in the attenuation law of high redshift galaxies (e.g. Reddy et al. 2016) by making the same assumptions in the radiative transfer as in MAGPHYS . Hayward & Smith (2015) used simulations of an isolated disc galaxy and major galaxy merger to demonstrate that MAGPHYS can reliably recover properties of galaxies virtually independent of viewing angle and evolutionary stage, even in cases in which merger-induced AGN activity contributes as much as 25 per cent of the system's total bolometric luminosity.

Building on this initial study, Smith & Hayward (2015) modified MAGPHYS to provide statistical estimates of galaxy star formation histories, by marginalizing over the default input libraries, and used similar simulations from Lanz et al. (2013) to test how well the known simulated star formation histories could be recovered. Smith & Hayward (2015) showed that MAGPHYS is able to derive realistic marginalized estimates of the star formation histories of isolated disc simulations, but found that the best-fitting SFHs were unreliable, varying with viewing angle, and showing spurious bursts that were not present in the actual SFH. Smith & Hayward (2015) also found that MAGPHYS was unable to recover realistic SFHs for major mergers, attributing this to the parametrized SFHs (exponentially declining, with bursts superposed) in the input libraries.

At the same time, there is a growing amount of work in the literature based on spatially resolved galaxy modelling and SED fitting, and the natural sources to begin with are bright, local galaxies which cover a large sky area. For example, the spatially resolved SED of the nearby galaxy M51 was studied by Mentuch Cooper et al. (2012) without using an energy balance model. More recently, Viaene et al. (2014) used a version of the MAGPHYS code (with a non-standard library including a slightly broadened range of dust temperatures) to model the SED of the nearby Andromeda galaxy (M31, originally studied using MAGPHYS by Groves et al. 2012, to investigate the source of dust heating). This was done both for the

galaxy as a whole and by decomposing the photometry into individual structural components (including the bulge, the ring, and the inner disc) as well as into individual resolution elements as small as 140 × 610 pc. Viaene et al. (2014) produced resolved maps of various parameters produced by the model and compared the parameters derived from the global photometry and with those obtained via the pixel-by-pixel fitting. Though the values derived in each case were comparable, a robust and direct comparison between the pixel-by-pixel values and the integrated properties is complicated, since for a variety of practical observational reasons, the area used to sum over the pixel-by-pixel values differs for each parameter (individual resolution elements with large parameter uncertainties were disregarded), and are therefore always smaller than the area used for the global photometry.

The recent work by Sorba & Sawicki (2015) highlighted the alarming prospect of a resolution-dependent systematic bias in stellar mass estimates for a sample of 67 nearby galaxies using just six bands of photometry from *GALEX* and SDSS (i.e. in the absence of far-infrared data), in the sense that integrated stellar masses were underestimated relative to the sum of the masses of the individual components. Sorba & Sawicki (2015) attributed this discrepancy to an 'outshining' bias, in which the youngest stars dominate the integrated emergent spectrum, and loss of information about the star formation history, and therefore mass-to-light ratio, in which the numerator is dominated by the less luminous old stellar population. This result is highly alarming, since if it is confirmed, it implies that the vast majority of known galaxies (i.e. those for which we are unable to decompose the photometry into individual resolution elements) have had their stellar mass content underestimated. Other works have found tentative evidence for similar resolution-dependent bias in dust masses derived for the Large Magellanic Cloud (Galliano et al. 2011), and for NGC 628 and NGC 6946 (Aniano et al. 2012). Elsewhere, Amblard et al. (2017) attempted a spatially resolved SED decomposition of two local early type galaxies (IC1459 and NGC2768) on sub-kpc scales from rest-frame UV to the far-infrared (including wavelengths up to 160 μm). Most recently, Jung et al. (2017) studied the difference in stellar mass, SFR, UV dust obscuration, and mass-weighted age recovered whether the integrated or resolved UV to near-IR photometry is used for parameter estimation (using a Monte Carlo Markov Chain sampler based on CB07 models), in order to investigate the radial dependence of the specific star formation rate in high-redshift galaxies. The recent work by Cibinel et al. (2015) suggested that identifying merging galaxies at high-*z* according to their SED-fitting derived stellar mass estimates is more robust than using single-band photometry, and there are many other works that have attempted to decompose the SEDs of spatially resolved galaxies (e.g. Baes et al. 2010; De Looze et al. 2012, 2014). In addition, recent studies of spatially resolved lensed galaxies (e.g. with ALMA; Dye et al. 2015; Swinbank et al. 2015) suggest that similar analyses may be possible out to the highest redshifts using forthcoming facilities.

Age gradients in the stellar populations of galaxies from integral field spectroscopy can used to critically differentiate between different formation mechanisms of early type galaxies (e.g. whether gas stripping, stellar feedback or major mergers were responsible for truncating their star formation). Given the vastly greater observational expense of spectroscopy relative to photometry, it is clearly desirable to reliably estimate the same properties from panchromatic photometry alone, since photometry will always be available for more galaxies than can be observed using integral field spectroscopy (even with new, wide-field, high-throughput spectrographs

such as MUSE, MaNGA and WEAVE; see Bacon et al. 2010; Dalton et al. 2012, 2014; Bundy et al. 2015, respectively).

Simulated data are ideal for investigating how well MAGPHYS can perform with spatially resolved data, since they present an idealized proving ground, free from nuisance observational effects (e.g. noisy photometry, different spatial resolution at different wavelengths, etc.), and where the true distributions of e.g. star formation, stellar mass, and dust mass are known. In this paper, we test the ability of MAGPHYS to produce reliable estimates of galaxy properties (including stellar mass, SFR, sSFR, stellar metallicity, $A_V$, $M_{dust}$, and mass-weighted age) at a range of different spatial scales varying from the integrated photometry to pixels 0.2 kpc on a side (similar to the highest resolution sampled in the nearby galaxy M31 by Viaene et al. 2014). Although Hayward & Smith (2015) found that MAGPHYS was able to infer global properties of simulated galaxies, such as the total SFR, from their integrated SEDs reasonably well, it is by no means guaranteed that a similar level of success will be achieved when employing MAGPHYS on a pixel-by-pixel basis. For example, the energy-balance criterion employed by MAGPHYS breaks down if the dust emission in a given pixel is predominantly powered by emission from stars located in other pixels. This must occur at some arbitrarily high resolution, but whether this assumption holds on the scales relevant for pixel-by-pixel SED modelling of galaxies is an open question.

In this work, we extend the analysis of Hayward & Smith (2015) by performing pixel-by-pixel SED modelling of a simulated galaxy to test how well MAGPHYS can recover the simulated galaxy's *spatially resolved* physical properties. In a companion paper (Hayward & Smith in preparation), we compare the MAGPHYS results with those obtained using simpler tracers (e.g. Hα luminosity-based SFR maps). The remainder of this paper is organized as follows. In Section 2, we describe the MAGPHYS model, alongside the simple modifications we have made to the fitting code. Section 3 contains our results, in which we compare the output produced by MAGPHYS with the known true parameters of the simulated galaxy as a function of the spatial scales that we probe. We discuss these results in Section 4, while Section 5 contains some concluding remarks. Throughout we adopt a standard cosmology with $H_0 = 71 \, \text{km} \, \text{s}^{-1} \, \text{Mpc}^{-1}$, $\Omega_M = 0.27$, and $\Omega_\Lambda = 0.73$.

## 2 METHODS

### 2.1 Synthetic images of a simulated galaxy

We employ galaxy images generated by performing dust radiative transfer on a 3D hydrodynamical simulation of an isolated disc galaxy. The approach has been described in detail in many previous works (e.g. Jonsson, Groves & Cox 2010; Hayward et al. 2011, 2012; Hayward & Smith 2015), so we will only summarize it briefly here.

First, we generate initial conditions for an isolated disc galaxy following Springel et al. (2005). The galaxy is composed of a dark matter halo, exponential stellar and gas discs, a stellar bulge, and a central supermassive black hole (BH). We analyse a single model galaxy, the 'M3' model presented in Lanz et al. (2014), whose properties (e.g. gas fraction and disc scalelength given its stellar mass) are designed to be representative of local galaxies (see Cox et al. 2008). For this work, we employ eight times the number of particles used in Lanz et al. (2014) to provide better sampling of young stars. The simulated galaxy's virial, stellar disc, gas disc, stellar bulge, and BH masses are $1.16 \times 10^{12}$, $4.2 \times 10^{10}$, $8 \times 10^9$, $9 \times 10^9$, and $10^5 \, \text{M}_\odot$, respectively. All other properties are identical

to those of the 'G3' model of Cox et al. (2008). The number of particles used to represent the dark matter halo, stellar disc, gas disc, and stellar bulge is $9.6 \times 10^5$, $4 \times 10^5$, $4 \times 10^5$, and $8 \times 10^4$, respectively. The gravitational softening lengths are 50 (200) pc for the gas and stellar (dark matter) particles.

Initial conditions in hand, we then evolve the simulated galaxy using a non-public version of the GADGET-3 smoothed particle hydrodynamics (SPH) code (Springel 2005).[1] The code directly accounts for the effects of gravity, hydrodynamics, and radiative heating and cooling. We account for the unresolved structure of the ISM, including the effects of supernova feedback, using the model of Springel & Hernquist (2003). Gas particles with a density greater than a threshold of $n \sim 0.1 \, \text{cm}^{-3}$ are assumed to form stars at a rate set by the volume-density-dependent form of the Schmidt–Kennicutt relation (Schmidt 1959; Kennicutt 1998). BH accretion and feedback is included following Springel et al. (2005) (modified Eddington-limited Bondi–Hoyle accretion and thermal 'quasar-mode' feedback), but this is unimportant for the simulation studied here. The initial stellar ages (which matter only for the radiative transfer calculations; see below) and stellar and gas metallicities are assigned following Lanz et al. (2014). Aging of the stellar population and enrichment of the ISM is followed self-consistently as the system evolves.

We evolve the simulated galaxy for 1 Gyr. As evident in Fig. 1, at this time, the galaxy is a thin disc with spiral arms and a notable bar; the latter two features develop self-consistently from an initially axisymmetric smooth disc. The global morphology of the galaxy is 'reasonable', although the ISM is unresolved on scales $\lesssim 100$ pc.

Using the outputs of the hydrodynamical simulation to specify the 3D distributions of sources of emission (star particles and the BH) and dust, we perform dust radiative transfer to forward-model spatially resolved spectral energy distributions (SEDs) spanning the UV–mm for seven viewing angles, ranging from face-on to edge-on (see Fig. 1). We employ the 3D Monte Carlo radiative transfer code SUNRISE (Jonsson 2006; Jonsson et al. 2010). For star particles with ages $> 10$ Myr, SUNRISE assigns single-age stellar population SEDs appropriate for their age and metallicity using STARBURST99 (Leitherer et al. 1999). For younger star particles, it employs the models of Groves et al. (2008), which account for the effects of H II regions and photodissociation regions (PDRs). However, for reasons detailed below, we assume a PDR covering fraction of 0. We assume an initial mass function from Kroupa (2001). The BH is assigned an SED using the luminosity-dependent templates of Hopkins, Richards & Hernquist (2007), which are based on observations of unreddened quasars. The gas-phase metal distribution in the hydrodynamical simulation is used to specify the dust distribution, assuming a constant dust-to-metal density ratio of 0.4 (Dwek 1998; James et al. 2002). To calculate the effects of dust absorption and scattering, Monte Carlo radiative transfer is performed using $10^7$ photon packets, which we have ensured is sufficient to maintain Monte Carlo noise (in the resulting integrated SED) of a few per cent or less.[2] The intrinsic dust grain properties are specified assuming the Milky Way $R = 3.1$ dust model of Draine & Li (2007). Dust temperatures are calculated assuming thermal equilibrium,

---

[1] Although we employ the traditional density-entropy formulation of SPH, this is not a concern, because Hayward et al. (2014a) demonstrated that the results of idealized, non-cosmological simulations of isolated galaxies and galaxy mergers performed using SPH are almost identical to those performed using the more-accurate moving-mesh hydrodynanics code AREPO (Springel 2010).

[2] Of course, there will always be some surface brightness below which the results are too noisy; we address this below.
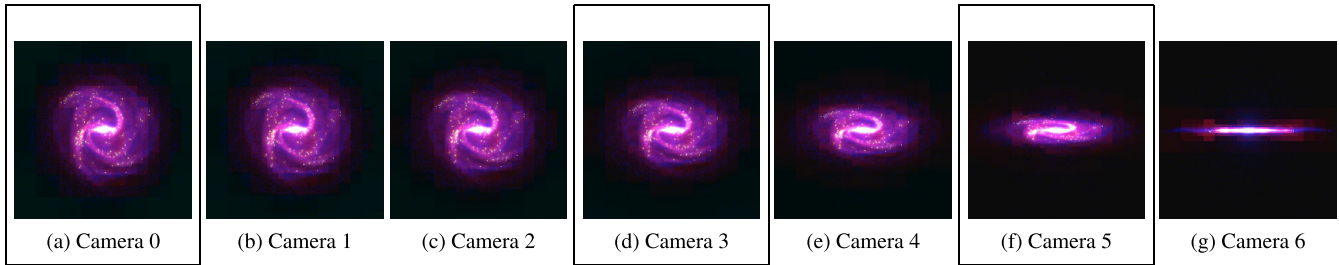
**Figure 1.** Composite images of the isolated disc simulation studied here, viewed from seven different viewing angles with particular wavelengths of interest mapped to different colours; $g'$ band is shown as blue, while 24 μm is green and 250 μm is red. The views which we have used for the MAGPHYS analysis (cameras 0, 3, and 5) are outlined.

and the resulting IR emission is propagated through the simulated ISM. Dust self-absorption is accounted for by iterating the photon packet propagation and dust temperature calculation steps until the dust temperatures are sufficiently converged, but given the modest optical depths in this simulated galaxy, this step is unimportant for this particular study.

Neglecting the physical uncertainties inherent in the hydrodynamical simulation, the most significant uncertainty in the radiative transfer calculations is the treatment of the sub-resolution ISM structure. We typically employ two extreme approaches to estimate the level of uncertainty that: (1) the cold clouds implicit in the Springel & Hernquist (2003) model have zero volume-filling factor and thus do not participate in the radiative transfer ('multiphase-on') and (2) the dust is uniformly distributed on sub-resolution scales (i.e. both the diffuse ISM and cold clouds contribute; we refer to this as 'multiphase-off'). When employing the latter assumption, we assume a PDR covering fraction of zero to avoid 'double-counting' dust. This issue has been discussed extensively in many previous works (e.g. Hayward et al. 2011; Snyder et al. 2013; Lanz et al. 2014; Hayward & Smith 2015; Safarzadeh, Hayward & Ferguson 2017), so we will not discuss it in detail here. We simply note that we employ the 'multiphase-off' assumption because (1) owing to the higher optical depths, recovery of galaxy properties is more challenging and (2) it is in principle possible to recover the total true dust mass because all dust implicit in the simulation emits thermal radiation, unlike in the 'multiphase-on' case. To check the robustness of our results to the sub-resolution ISM structure, we re-ran the SUNRISE calculation with the 'multiphase-on' assumption and fit the 100 × 100 camera 0 image. Although the results quantitatively differed from the multiphase-off case, as they should (e.g. the true attenuation is less in the multiphase-on case, and this is also true for the recovered values), the conclusions were unchanged.

As noted above, the results of our calculations consist of spatially resolved UV–mm SEDs for the simulated galaxy viewed from seven different viewing angles (although we only analyse three of them in detail in this work). We set the field-of-view to 50 kpc and used 500 × 500 pixels, yielding an intrinsic image resolution of 100 pc (which is approximately the smallest physical scale resolved in the GADGET-3 simulations).

The SEDs predicted using simulations such as that studied here have been demonstrated to be consistent with e.g. local 'normal' galaxies (Jonsson et al. 2010), local (ultra-)luminous IR galaxies (Younger et al. 2009; Lanz et al. 2014), high-redshift ULIRGs (e.g. Hayward et al. 2011, 2012; Roebuck et al. 2016), and obscured AGNs (Snyder et al. 2013; Roebuck et al. 2016), post-starburst galaxies (Snyder et al. 2011), and compact quiescent galaxies

(Wuyts et al. 2010). Thus, despite the simulations not being perfectly representative of real galaxies, it is reasonable to employ them for 'controlled experiments' such as this study (see also e.g. Hayward et al. 2014b; Michałowski et al. 2014; Hayward & Smith 2015; Smith & Hayward 2015) in which we attempt to recover physical quantities from (synthetic) observables and compare the results with the 'ground truth' values, which is not possible when studying real galaxies.

### 2.2 The MAGPHYS model

MAGPHYS is described in detail in da Cunha et al. (2008), however we will provide a brief overview here. MAGPHYS uses an empirical but physically motivated model to produce consistent SEDs of galaxies from the rest-frame ultraviolet to the far-infrared. It does this by using a simple two-component dust model from Charlot & Fall (2000) to absorb photons in the stellar birth clouds and diffuse interstellar medium, and re-radiate this energy in the far-infrared. MAGPHYS includes a library of optical to near-infrared stellar spectra based on 50 000 exponentially declining star formation histories (with random bursts superposed) derived using the latest version of the Bruzual & Charlot (2003) stellar population libraries (the 'CB07' library, unpublished), assuming an initial mass function from Chabrier (2003), and a range of metallicities between $0.0 < Z < 2.0$ (in solar units). This library is consistently linked to a dust library containing 50 000 dust emission SED models (each consisting of multiple continuum components associated with dust grains with a range of sizes and temperatures, as well as emission lines from polycyclic aromatic hydrocarbons) according to an energy balance criterion. The energy balance criterion specifies that the energy absorbed from starlight by dust primarily at UV/optical wavelengths is re-radiated in the far-infrared, and this ensures that the model SEDs are physically consistent across the full wavelength range. While this criterion is reasonable for modelling whole galaxies, it may not be the case for regions within galaxies, since emission from neighbouring areas can dominate the heating of dust in a given region. It is therefore essential to test how well MAGPHYS works in the spatially resolved regime.

MAGPHYS produces model photometry based on passing the emergent SED from each combination of the libraries satisfying the energy balance criterion through the filter curves appropriate for the available observations. These model fluxes are then compared to the empirical values and uncertainties using the $\chi^2$ algorithm. By assuming that $P' \propto \exp(-\chi^2/2)$, the relative likelihood for each star formation history (or dust emission SED model) in the library is then recorded and used to produce marginalized probability distribution functions (PDFs) for each parameter in the model.

In Smith & Hayward (2015), we described modifications to MAG-PHYS to allow these probabilities to be output for each star formation history in the stellar library, enabling e.g. average star formation histories to be determined. Outputting these data also allows PDFs to be derived in post-processing without having to further modify and re-run the MAGPHYS fitting (which is reasonably CPU-intensive, taking ∼8 min per galaxy on a single 2.5 GHz processor), by taking the input parameters from the MAGPHYS library of stellar SEDs (which also include e.g. metallicity, mass-weighted age, and $A_V$[3]), along with the marginalized probability distribution for each. In this way, we can produce best fit as well as median-likelihood parameter estimates, along with uncertainties estimated using the 16th and 84th percentiles of the PDF, in exactly the same way as the default version of the code does, but for a wider range of parameters, since the supplied version of MAGPHYS treats metallicity and mass-weighted age as nuisance parameters, and does not include $A_V$ values (though they can be trivially engineered from the spectral libraries). This can all be done with minimal modification of the fortran source code, requiring only the straightforward modifications to output a list of the probabilities for each SFH.

In this way, we can use MAGPHYS to estimate stellar metallicities and ages based on the full range of multiwavelength photometry, a step forward relative to recent works based on optical photometry alone (e.g. Smail et al. 2001; Lee et al. 2007; Carter et al. 2009; Sanders, Levesque & Soderberg 2013; Acquaviva 2016, though see also Amblard et al. 2017). It is generally recognized that the best metallicity and age estimates can only be obtained through deep spectroscopy (e.g. Poggianti et al. 2001), but it is potentially very useful if it is possible to obtain reliable metallicities from photometry alone. Though the benefit of including far-infrared data for estimating stellar metallicities and ages may not be initially clear, far-infrared data can potentially play a key role in breaking the age–metallicity degeneracy (e.g. Worthey 1994; Carter et al. 2009), since galaxies dominated by old stellar populations are in general far less luminous at far-infrared wavelengths than their younger counterparts. In this work, we therefore also perform exploratory tests to uncover the extent of the MAGPHYS formalism's ability to recover these non-standard outputs.

### 2.3 SED fitting using MAGPHYS

The simulation data cubes (which are analogous to integral field spectrograph data, i.e. they have two spatial dimensions that correspond to the 2D projected surface of the galaxy for a given camera angle and a third dimension that corresponds to wavelength) have an intrinsic spatial resolution of 500 × 500 pixels, each 0.1 kpc in size. We rebinned the emergent photometry by resampling the spatial dimensions of the data cubes into lower resolution versions 250, 100, 50, 20, 10, 5, 2, and 1 pixels on a side (corresponding to spatial resolutions of 0.2, 0.5, 1.0, 2.5, 5.0, 10, 25, and 50 kpc), and fit each individual element of the resulting arrays of photometry independently using MAGPHYS. This means that for each viewing angle, we performed a total of 75 530 individual SED fits requiring approximately $10^4$ CPU-hours for each. In order to see how our results vary depending on viewing angle, we applied the model to

cameras 0, 3, and 5, which are oriented such that $(\theta, \phi) = (0°, 0°)$, $(45°, 0°)$, and $(75°, 0°)$ for the three cameras, respectively,[4] with the galaxy's disc being oriented along the *xy* plane. Broadly speaking, camera 0 views the disc face-on, while camera 5's view is close to edge-on, with camera 3 in between.

In this analysis, we arbitrarily choose to use 21 bands of photometry, generated by convolving the emergent spectra at each location with the relevant filter curves. The bands we include are the following: FUV and NUV data from *GALEX* (Martin et al. 2005), *ugriz* bands from the Sloan Digital Sky Survey (York et al. 2000), *J*, *H*, and *K* band near-infrared filters from the UK Infrared Deep Sky Survey (UKIDSS; Lawrence et al. 2007), as well as 3.6, 4.5, 5.8, 8.0, 24, and 70 μm filters from the IRAC (Fazio et al. 2004) and MIPS (Rieke et al. 2004) instruments on the *Spitzer Space Telescope* (Werner et al. 2004), plus 100, 160, 250, 350, and 500 μm transmission functions for the PACS (Poglitsch et al. 2010) and SPIRE (Griffin et al. 2010) instruments on the *Herschel Space Observatory* (Pilbratt et al. 2010). The synthetic images that are produced by the simulations do not contain photometric uncertainties; however, in order to be able to fit the emergent photometry with MAGPHYS, we follow Smith & Hayward (2015) and assume a signal-to-noise ratio of five in every photometric band.

## 3 RESULTS

In this section, we will show the results of our MAGPHYS fitting in a range of different ways, in a bid to critically gauge how well MAGPHYS can perform in this challenging scenario. In the main body of the paper, we include the results for the face-on simulation (camera 0), while in the appendices we include selected analogous figures derived based on the model photometry for the other viewing angles. We will discuss how well MAGPHYS recovers each of seven parameters (stellar mass, SFR, specific SFR, dust mass, stellar metallicity, $A_V$, and mass-weighted age) in turn, and as a function of resolution in the next subsections. First, we begin by quantifying what fraction of the time MAGPHYS is able to produce good fits to the data.

### 3.1 Can MAGPHYS produce good fits to spatially-resolved data?

MAGPHYS is designed using an empirical, but 'physically motivated' model to describe the integrated properties of galaxies; this idealized model may therefore not be applicable to the spatially-resolved case. However, the MAGPHYS model is not strictly correct in the integrated case either, though we have shown (Hayward & Smith 2015; Smith & Hayward 2015) that this does not preclude it from producing reliable results. One key test that we must make before we can even begin to address whether the results it produces are sensible, is to determine whether the MAGPHYS model can produce statistically acceptable fits to the data. We do this using the $\chi^2$ criterion discussed in Smith et al. (2012), which provides a means of determining a $\chi^2$ threshold that depends only on the number of bands used in the fitting, above which there is a chance of less than 1 per cent that the data are consistent with the model. Since we include 21 photometric bands in our fitting, we identify 'good fits' as those which have $\chi^2 < 30.6$.

Fig. 2 shows the fraction of good fits as a function of radial separation from the centre of the galaxy for the five highest resolution runs (ranging from 250 × 250 to 10 × 10, with colours as shown

---

[3] We note that the values of $A_V$ used in this analysis are calculated by comparing the fluxes transmitted by the intrinsic and transmitted spectra through the *V* band filter curve, both for the MAGPHYS libraries, and for the model galaxy data cubes.

[4] We adopt the notation that $\theta$ and $\phi$ represent the polar and azimuthal angles, respectively.
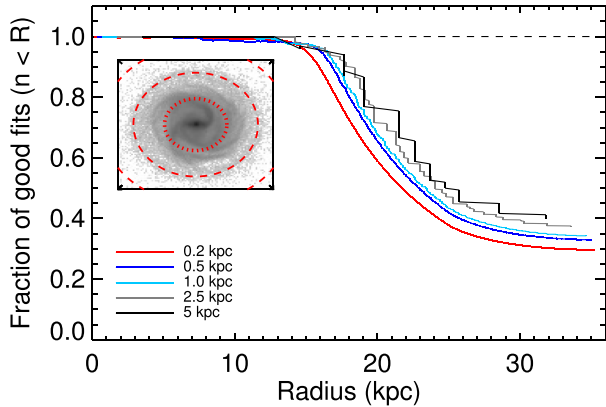
**Figure 2.** Fraction of good fits within each radius, shown for spatial resolutions 250, 100, 50, 20, and 10 pixels on a side (corresponding to 0.2, 0.5, 1.0, 2.5, and 5.0 kpc, as detailed in the legend). To give some idea of the physical scale, the inset grey-scale image shows the true stellar mass distribution and is overlaid with circles with radii of 10, 20, and 30 kpc, shown as the red lines (dotted, dashed, and dot–dashed, respectively). The $r$-band effective radius is 5.7 kpc. The pixels for which we do not obtain good fits contain a maximum of 2.3 and 1.0 per cent of the total stellar mass and SFR, respectively.
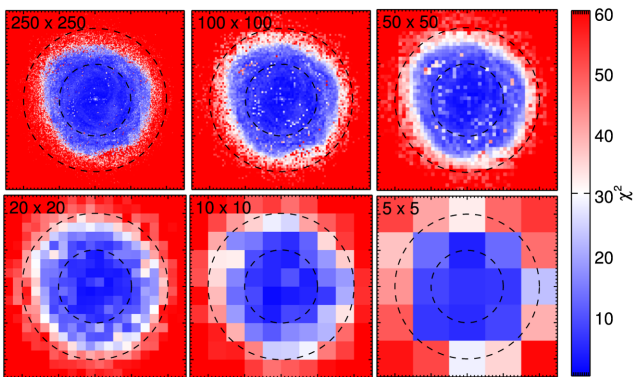


**Figure 3.** Maps showing the best-fitting values of $\chi^2$ as a function of position for six of the different resolution runs, ranging from the $250 \times 250$ pixel (0.2 kpc resolution) to the $5 \times 5$ (10 kpc resolution) run. The bar to the right indicates the colour scale, which is common to each panel, and which is centred on $\chi^2 = 30.6$, the cut-off value that delineates acceptable and unacceptable fits. In this scheme, the pixels for which a good fit was obtained are shown in blue (the bluer, the lower the $\chi^2$), while the rejected fits are shown in red, and those close to the threshold are white. Dashed circles indicate the regions within 10 and 20 kpc from the centre of the map, which is 50 kpc on a side in every case.

in the legend to the lower left). The fraction of good fits is a strong function of radius, and we are able to fit the vast majority of pixels ($\geq$99 per cent, in all runs) within 10 kpc (indicated by the dotted red line on the inset image of the true stellar mass distribution), while that figure drops to between 59 and 77 per cent of the pixels within 20 kpc (dashed red line in the inset), and the fraction of good fits is lowest for the higher resolution runs at large separations. To put these values in further context, the $r$-band effective radius of the galaxy is 5.7 kpc, and 99 per cent of the $r$-band light is emitted within 19.2 kpc. The pixels for which we do not obtain good fits contain a maximum of 2.3 per cent of the total stellar mass and 1.0 per cent of the total SFR.

In Fig. 3, we look at this in more detail for the six highest resolution runs, showing the best-fitting $\chi^2$ value as a function of position

on the map, colour coded such that good fits are in blue, and fits that were rejected by our $\chi^2$ criterion are shown in red, with increasingly strong colour indicating how far away from the threshold they are. The lack of spiral structure in the blue parts of these figures offers encouragement MAGPHYS is working as expected across a broad range of structure present in the galaxy. As noted above, the vast majority of the bad fits are in the faint outer regions of the disc, where the simulations begin to encounter Monte Carlo effects due to the quantization of the photon packets (see discussion of $A_V$ in Section 3.7.3, below). Examining the results of the MAGPHYS fitting of these unacceptable pixels does not reveal any one particularly discrepant wavelength regime providing the dominant source of the $\chi^2$, rather a steady progression towards worse $\chi^2$ with increasing distance from the centre.

In the coming sections, we will show parameter maps and scatter plots for each parameter that we attempt to recover; in all of these we will only show those pixels for which we are able to obtain acceptable fits to the data, and as we shall see, we are able to recover a range of total/effective properties very well. Although our work is based on the MAGPHYS libraries built using the CB07 stellar templates, we re-ran a subset of the fits using the Bruzual & Charlot (2003) libraries currently recommended on the MAGPHYS website, finding no significant differences in our results which follow.

### 3.2 MAGPHYS recovery of stellar mass, $M_{\text{stars}}$

Fig. 4 shows the fidelity of the stellar mass recovery in three different ways. Fig. 4(a) shows images of the true and recovered stellar mass in the left and centre columns, respectively, with the difference between the two (MAGPHYS - True) indicated in the right-hand column. The spatial resolution decreases from 0.2 kpc in the upper row to 10 kpc in the bottom row. Fig. 4(b) shows the true and MAGPHYS values plotted directly against one another for the full range of resolutions; in the top row (corresponding to the highest spatial resolutions) we show only a 2D histogram of the best-fitting values (with the colour bar linear in the logarithm of the number of pixels in each bin, between $0 < \log N < \log N_{\text{max}}$, and with a typical error bar on an individual data point shown in the bottom right), while for the lower row we show the best-fitting values with uncertainties on the MAGPHYS values based on the 16th and 84th percentiles of the stellar mass PDF. Fig. 4(c) shows the radial dependence of the stellar mass (true values on the left, recovered MAGPHYS values on the right). For the $250 \times 250$, 0.2 kpc resolution scenario, the median $M_{\text{stars}}^{\text{true}} - M_{\text{stars}}^{\text{magphys}} = -0.08$ dex with 68 per cent of the data within 0.16 dex across the whole mass range, equivalent to the $1\sigma$ interval in the limit of Gaussian statistics.

It is clear that MAGPHYS produces excellent estimates of stellar mass, both in the unresolved case (as demonstrated in Hayward & Smith 2015), and now shown here in the resolved case, at resolutions of up to 0.2 kpc. MAGPHYS is able to reliably recover best-fitting stellar mass values as low as $10^4\,\text{M}_\odot$, and produces good fits at the vast majority of locations across the disc (as discussed in Section 3.1). The spiral arm structure is apparent in both the true and MAGPHYS mass maps in Fig. 4(a), while the MAGPHYS values are located along the 1:1 line in each panel of Fig. 4(b), and the recovery of the radial dependence shown in Fig. 4 (c) is also excellent.

As mentioned in Section 1, the work by Sorba & Sawicki (2015) suggested that the stellar masses estimated for galaxies with only integrated photometry may have been underestimated relative to the sum of the individual components. In the left column of Fig. 5, which the three rows corresponding to the three viewing angles chosen for this study, we test for the influence of resolution on the
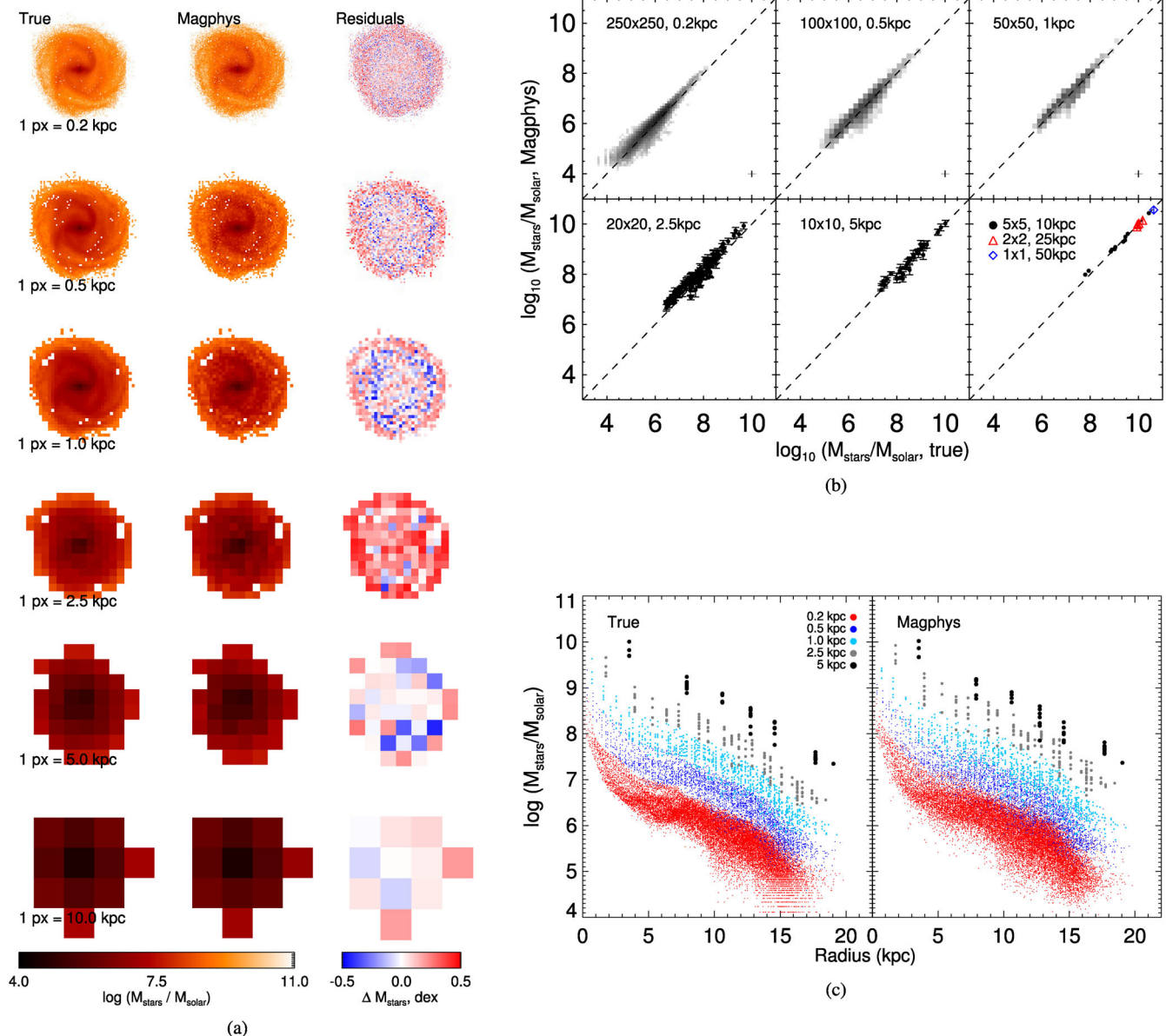
**Figure 4.** Recovery of stellar mass for camera 0. In this and similar figures below, only those pixels for which MAGPHYS obtains good fits according to the $\chi^2$ criterion defined in Smith et al. (2012) are shown. In panel (a), we show three columns of images, detailing the true stellar mass distribution (left), and the MAGPHYS estimates (centre) with spatial resolution decreasing from top (0.2 kpc pixels) to bottom (10 kpc pixels), as labelled in bottom left corner of the left column. The colour bar (shown at the bottom) has been chosen to represent values in the range $4 < \log(M_{stars}/M_{\odot}) < 11$. The right-hand column shows the difference between the MAGPHYS estimates and the true values, in dex, with the colour bar at the bottom indicating the scale. In panel (b), located on the upper right-hand side, we show the recovered stellar masses as a function of the true values taken from the simulations, with different resolutions shown in each panel, as labelled in the legend. The diagonal dashed line in each panel indicates the 1:1 relation. The top three panels are shown as a 2D histogram with a colour scale linear in the logarithm of the bin occupancy, ranging from $0 < \log N < N_{max}$ and a typical error bar shown in the lower right corner, while in the lower panels the comparatively lower number of pixels allows us to also overlay the uncertainties returned by MAGPHYS, shown by the vertical error bars. In panel (c), we show the variation of the stellar mass as a function of the radial distance from the centre of the galaxy in kpc, with the different resolutions shown as different colours detailed in the legend. The true values are shown in the left-hand panel, while the corresponding MAGPHYS values are shown to the right. At all resolutions, the stellar masses of individual pixels are recovered extremely well, and consequently, so are the projected stellar mass maps and radial distributions.

total stellar mass obtained using MAGPHYS, by calculating the sum of the individual masses at each resolution (including propagating the error bars), and comparing with the true stellar mass (shown as the horizontal dashed line). Fig. 5 shows that there is no strong evidence for a resolution-dependent bias in the stellar mass estimates;

if there is a discrepancy it is located at the spatially resolved end (i.e. the opposite of what was found by Sorba & Sawicki 2015), where the error bars are inconsistent with the true stellar mass (though as discussed above, the 'discrepancy' is less than 0.1 dex) and this trend is consistent for each of the three viewing angles. We will
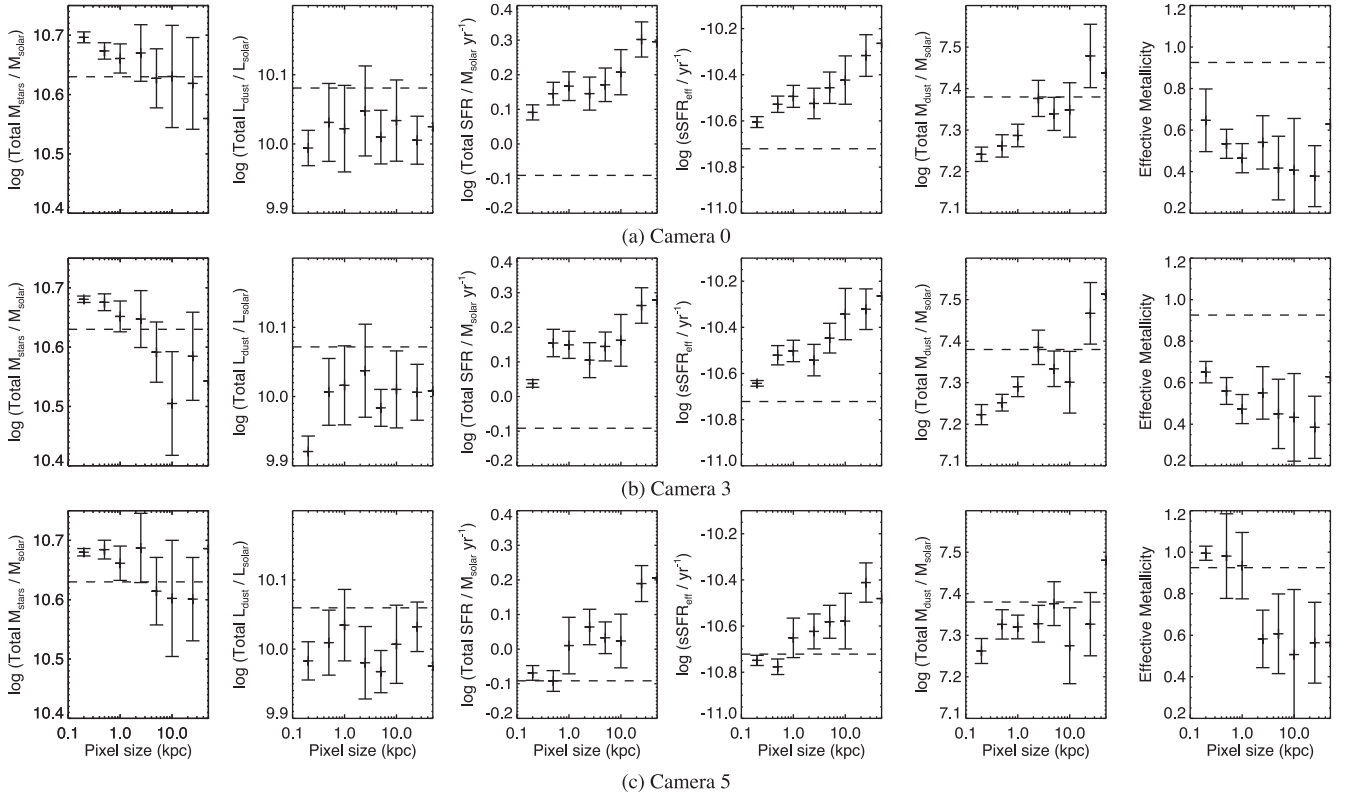
**Figure 5.** Plots showing (from the leftmost to rightmost column) the total stellar mass, dust luminosity, SFR, effective sSFR, total dust mass, and effective stellar metallicity, obtained by summing the values recovered by MAGPHYS for each pixel, as a function of the pixel size. The true values taken from the simulation are shown as the horizontal dashed lines. Stellar mass is recovered superbly at all resolutions. The SFR and sSFR values are overestimated somewhat, increasingly so at lower resolution, with maximum overestimates of ~0.4 dex. The dust mass is underestimated by ≲0.2 dex at the highest resolutions and recovered to within 0.1 dex for pixel sizes greater than a few kpc. The metallicity recovery is poor except for the highest-resolution, edge-on photometry.

return to this figure in the coming sections, with reference to the other panels.

### 3.3 MAGPHYS recovery of dust luminosity

The panels of Fig. 6 are similar to Fig. 4, however they now detail the extent of our ability to recovery the dust luminosity across the disc. It is unsurprising, given the 21-bands of SNR = 5 photometry that we have assumed in our numerical experiment, that our tests show that MAGPHYS produces very high fidelity dust luminosities across the whole disc, and even down to luminosities as low as $10^3\,L_\odot$. We are able to clearly make out the spiral structure in the recovered parameter maps (shown in the centre column of Fig. 6 a) and in the obvious radial structures present in the true data cube and in the MAGPHYS recovered values (Fig. 6 c).

For the 250 × 250 test, the median $L_{\rm dust}^{\rm true} - L_{\rm dust}^{\rm magphys} = 0.12$ dex, reflected by the light blue colour of the majority of the pixels in the right-hand column of Fig. 6 (a). This value is very similar to the one found for the integrated case discussed in Hayward & Smith (2015), however we now show virtually identical behaviour in the spatially resolved case. In the second columns of Fig. 5, we investigate the possibility of resolution bias in estimates of the total far-infrared luminosity, by summing the dust luminosity in each of the individual pixels and propagating the error bars at each individual resolutions (as for the stellar mass analysis discussed above), finding no evidence for such an effect.

### 3.4 MAGPHYS recovery of SFR

In Fig. 7 we now compare the MAGPHYS SFR estimates with the true values. Fig. 7 again reveals that, despite each individual pixel being fit independently of the neighbouring pixels, the spiral arm structure is again quite clear in the recovered SFR map, despite the increased scatter between the MAGPHYS and true SFRs shown in the right column of Fig. 7(a) and Fig. 7(b) relative to the situation for the stellar masses. The spiral arm structures visible in Fig. 7(a) are also visible as structures in the true radial SFR values – shown in the left-hand panel of Fig. 7(c) – though they are washed out in the MAGPHYS values. However, the trend of decreasing SFR with increasing radius is clearly apparent in the MAGPHYS results.

Though the scatter in individual SFRs is considerable (especially fitting to pixels scales <0.5 kpc), the total SFR recovered at each resolution compares reasonably well with the true total SFR (0.81 $M_\odot\,{\rm yr}^{-1}$). These values are shown in the second column of plots in Fig. 5, where we find a modest offset of 0.1–0.3 dex between the true values and the MAGPHYS estimates (consistent with the values found for a broader range of simulation time-steps in Hayward & Smith 2015). We also find evidence for a resolution dependence, with the low spatial resolution values having the largest overestimates of the true total SFR, though the offset is driven primarily by the highest resolution data point, which we have already identified as potentially problematic in Fig. 7(b). This trend of increasing recovered SFR with increasing pixel size remains apparent for each viewing angle to the disc.
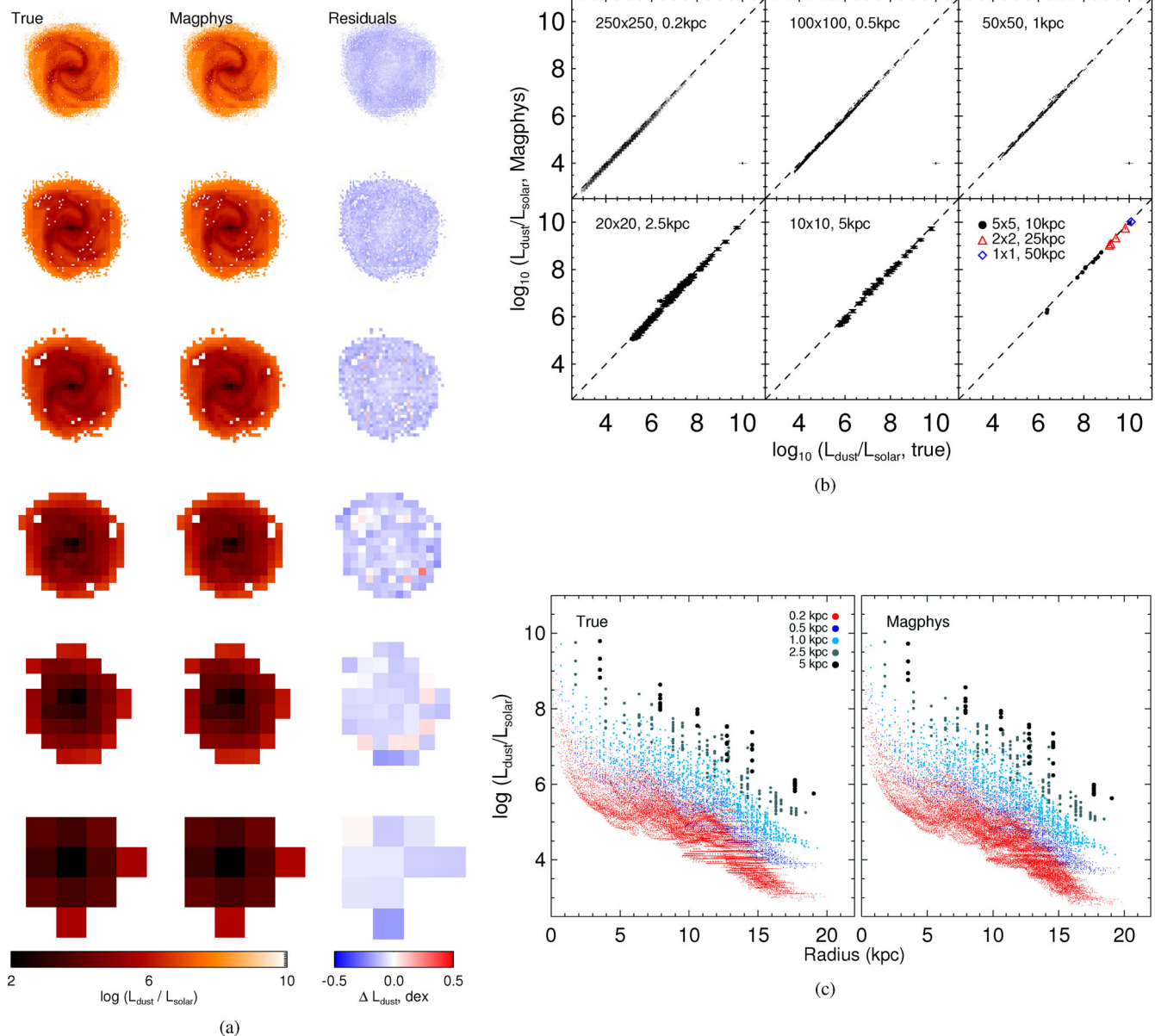
**Figure 6.** Recovery of dust luminosity for camera 0. The colour scales for the images showing the true and MAGPHYS -estimated luminosity distributions are given by the colour bars at the bottom of each column of panel (a). For more details, see the caption of Fig. 4. The details of the dust luminosity maps (e.g. spiral arms) are well recovered by MAGPHYS , as are the radial profiles. At all resolutions, the dust luminosity contained in individual pixels are recovered very well.

Two main regions of discrepancy are apparent. The first is in the outer regions of the spiral arms, where the MAGPHYS results suggest a halo of low-level star formation that is not seen in the true values (this feature is particularly visible as an annular excess around the edge of the galaxy in the 3rd and 4th rows of Fig. 7 (a), corresponding to pixel sizes of 1 kpc and 2.5 kpc, but it is also apparent in the other panels). The second is in the inter-arm regions, where MAGPHYS returns considerably higher values than the ground-truth. The left-hand panel of Fig. 8 highlights that these regions are predominantly the parts of the galaxy surface with the lowest effective dust temperatures. To ensure that these discrepancies are not due to the influence of the choice of dust temperature priors in the default MAGPHYS library, and in an attempt to marginalize over the multi-component dust model MAGPHYS assumes to build the dust SEDs, in

the right-hand panel of Fig. 8, we show a comparison between the range of *effective* dust temperatures of the FIR SEDs of individual pixels of the model galaxy (filled histogram) and those of the individual MAGPHYS IR SED templates (outlined histogram), with the priors on the ISM and birthcloud temperatures also overlaid (as blue dotted and red dashed histograms, respectively). The effective temperatures are estimated based on remapping the 70/160 μm flux ratio on a pixel-by-pixel basis, assuming an isothermal model with an emissivity index $\beta = 1.82$ following Smith et al. (2013), and the values reveal that the prior is sufficiently broad for our purposes.[5]

---

[5] This may seem at odds with there being a gap in the distributions of *isothermal* temperature for the ISM and birthcloud components shown in
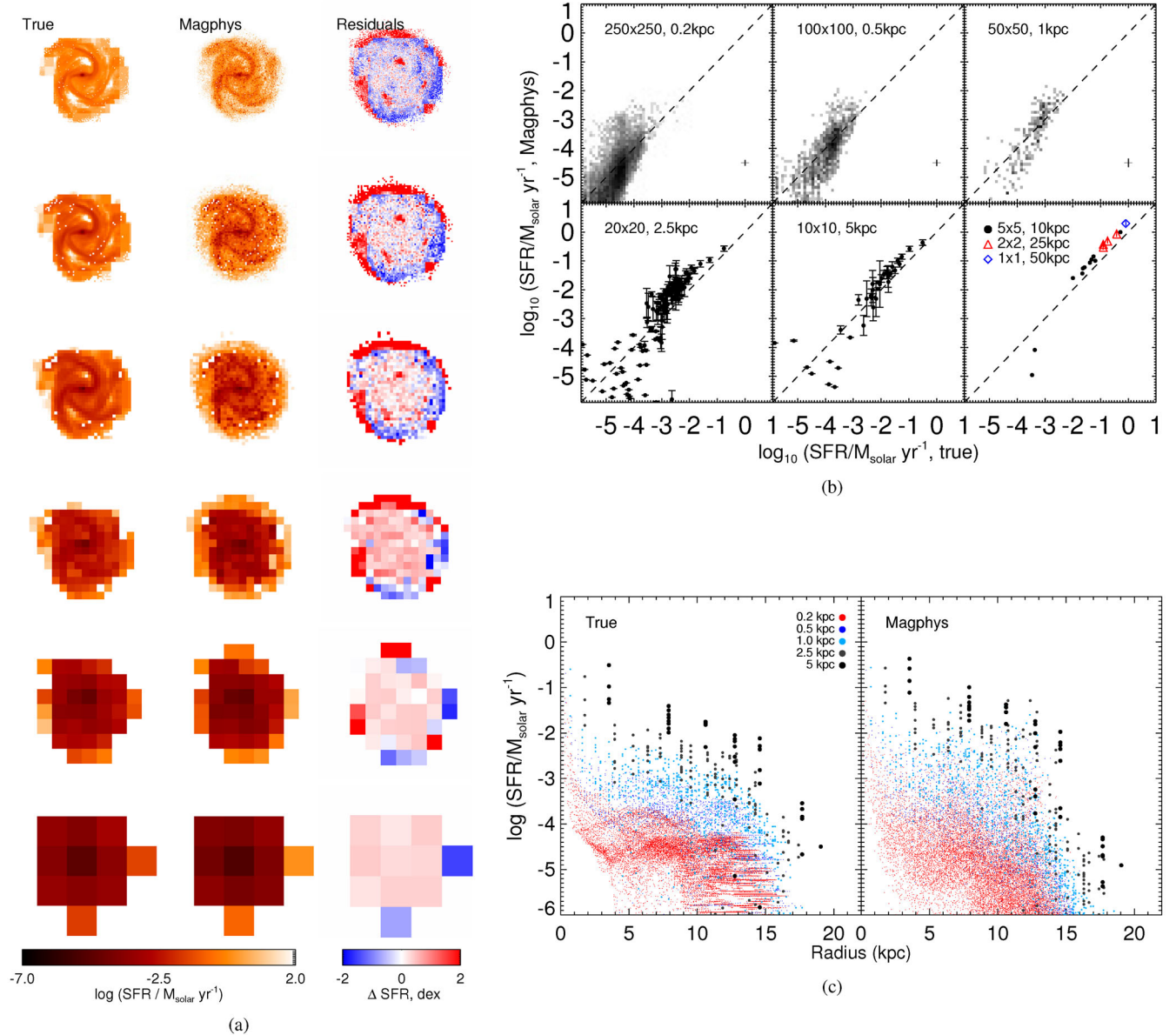
**Figure 7.** Recovery of SFR for camera 0. In panel (a), the colour scales used for the SFR and residual images are as detailed in the bars at the bottom of the corresponding column. For more details, see the caption of Fig. 4. The SFRs of individual pixels are typically recovered well for pixel scales $\gtrsim 1$ kpc, although the true values are slightly systematically overestimated, resulting in the systematic overestimate of the total SFR evident in Fig. 5. For smaller scales, there is considerable scatter around the one-to-one relation (although the recovery of the total SFR is better at these resolutions; see Fig. 5). Moreover, MAGPHYS overestimates the SFR in the inter-arm regions. Although the radial dependence of the SFR is approximately recovered, at the highest resolutions, detailed features are lost.

It is possible that the dust heating in these regions is being misinterpreted by MAGPHYS as from young stars within these pixels rather than the diffuse interstellar radiation field, which is dominated by neighbouring pixels, leading to the overestimated SFRs in these regions. These regions are prime locations where the assumption of *within-pixel* energy balance may break down, since in the lowest sSFR pixels, stars lying in neighbouring pixels are likely to contribute significantly to the dust heating. As expected, such discrepancies disappear when sufficiently large pixels are employed because as the pixel size is increased, the minimum values in the true SFR maps (ignoring pixels with zero star formation) increases and thus the within-pixel energy balance assumption becomes increasingly valid.

Fig. 8, however recall that the two components have different emissivity indices, and that the MAGPHYS far-infrared library – which is described fully in da Cunha et al. (2008) – is more complicated than simply a sum of two components with adjustable temperatures shown in the right-hand panel of Fig. 8.

### 3.5 MAGPHYS recovery of sSFR

Having investigated the recovery of the MAGPHYS SFR and stellar mass in the previous sections, we now investigate the recovery of
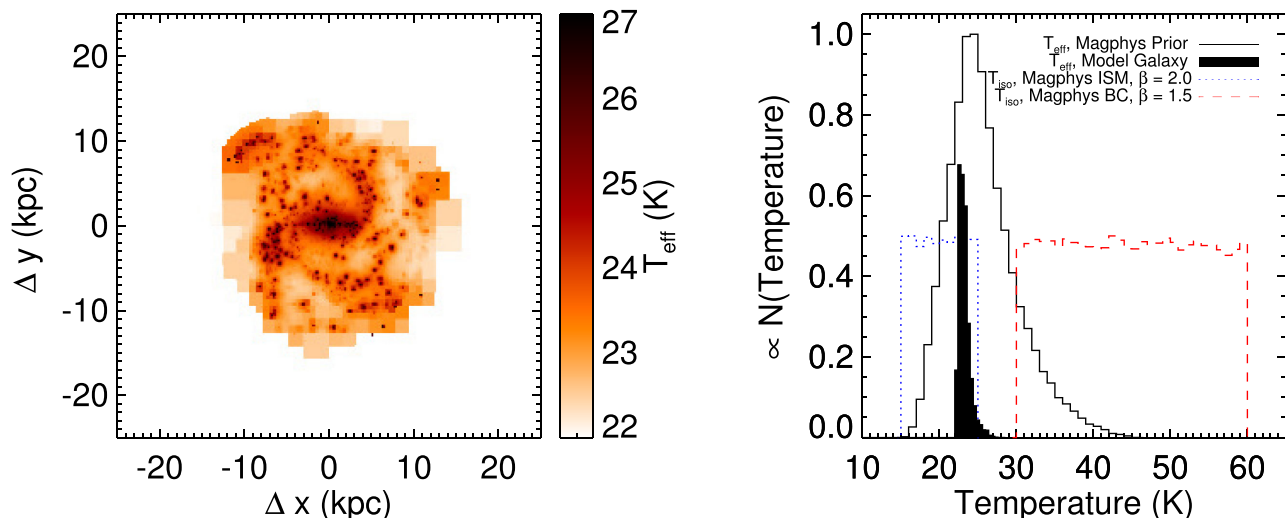
**Figure 8.** Left: map of the effective temperature of the far-IR dust SED, estimated from the ratio between the MIPS 70 and PACS 160 μm model fluxes and assuming an emissivity index of 1.82 from Smith et al. (2013). The temperature scaling is indicated by the colour bar to the right, with values over the range $22 < T_{\rm eff} < 27$ K, spanning the full range of effective dust temperatures in the disc. The dust around young star particles is hottest, whereas that in inter-arm regions, which is primarily heated by the diffuse interstellar radiation field, is coldest. Right: A comparison between histograms showing the range of *effective* dust temperatures spanned by the default MAGPHYS far-infrared library (black solid line), and the effective temperatures of the SEDs of individual pixels in our highest resolution simulation (i.e. the values shown in the left panel, shown as the filled black hisogram). Also overlaid are the *isothermal* temperature distributions of the hot and cold components of the MAGPHYS library (red dashed and blue dotted histograms, respectively). This comparison demonstrates that while the individual components may have a discontinuous prior distribution, the prior of the overall effective dust temperature in MAGPHYS is sufficiently broad.

the specific star formation rates. The spiral arm structures are visible in the maps of the MAGPHYS values by virtue of their elevated sSFR relative to the nuclear and inter-arm regions in Fig. 9(a), while Fig. 9(b) and (c) highlight the very large spread in the recovered values about the 1:1 relation, though this is most apparent in the highest-resolution tests with pixels <1 kpc in size. The values determined for the low-spatial resolution cases (pixels ≥1 kpc) are more consistent with the true values taken from the simulations.

The inter-arm and especially the outer regions of the disc that were also problematic for the SFR recovery represent some of the most challenging areas. These are the regions where the effective dust temperature is lowest, and where the energy balance criterion is perhaps more of a hindrance due to the importance of neighbouring regions for the dust energy budget.

The plots in the centre column of Fig. 5 show the resolution dependence of the effective sSFR (obtained by dividing the total SFR by the total stellar mass, with both estimated by summing over all of the good fits at each of the resolutions). As expected based on the stellar mass and SFR values (and based on the results of Hayward & Smith 2015), we find evidence for a modest offset of up to ∼0.3 dex, and possible evidence for a resolution-dependent bias, however – as for the SFR – this is primarily driven by the highest resolution data points.

### 3.6 MAGPHYS recovery of dust mass, $M_{\rm dust}$

We now consider how well MAGPHYS is able to recover the spatial distribution of the dust mass.[6] Fig. 10(a) reveals that MAGPHYS performs very well at this task, with the spiral structures visible in the true

---

[6] As in Hayward & Smith (2015), the dust emissivities assumed by the two codes differ; in MAGPHYS, the emissivity is normalized by $\kappa_{850\,\mu m} = 0.77\,{\rm g}^{-1}\,{\rm cm}^2$ following Dunne et al. (2000), whereas the MW dust model used in the simulations has $\kappa_{850\,\mu m} = 0.38\,{\rm g}^{-1}\,{\rm cm}^2$. Conse-

dust mass maps apparent and well-defined in the MAGPHYS estimates. MAGPHYS is able to estimate dust masses as low as $10\,{\rm M}_\odot$ in the outer regions of the highest resolution maps. Although there is little or no evidence for bias in the overall dust mass estimates, or in the more massive pixels (irrespective of their size), Fig. 10(a) and (b) highlight that there is a mass-dependent bias, such that the lowest dust masses are underestimated by ∼1 dex. Fig. 10(a) shows that the regions where this occurs are primarily in the outer regions of the galaxy, which are bright blue in the residual maps; these pixels are located at radial distances >10 kpc, where Fig. 8 indicates that the effective dust temperature is lowest. This discrepancy is not due to the MAGPHYS dust temperature priors, which include models for the ambient ISM as cold as 15 K, considerably colder than the coldest regions of the isolated disc simulation that we use in this work (after accounting for the difference in $\beta = 1.82$ used by MAGPHYS and the intrinsic $\beta = 2.0$ of the dust grain model assumed in the radiative transfer calculations). Remarkably, the spiral structures visible in the true radial distributions of dust mass within 10 kpc at the highest spatial resolution (shown as the red points in Fig. 10 c) are also apparent in the MAGPHYS estimates.

The total dust mass recovered estimated as a function of spatial resolution is shown in Fig. 5, revealing that at spatial scales ≳ 1 kpc, the total dust mass is recovered well, while at higher resolution (i.e. smaller pixel sizes) the total dust mass is slightly underestimated by around 0.15 dex, presumably due to the large number of low-dust-mass pixels at large distances from the nucleus.

### 3.7 MAGPHYS recovery of non-standard parameters

In this section, we analyse the extent of MAGPHYS' ability to recover the additional parameters – metallicity, $A_V$ and mass-weighted

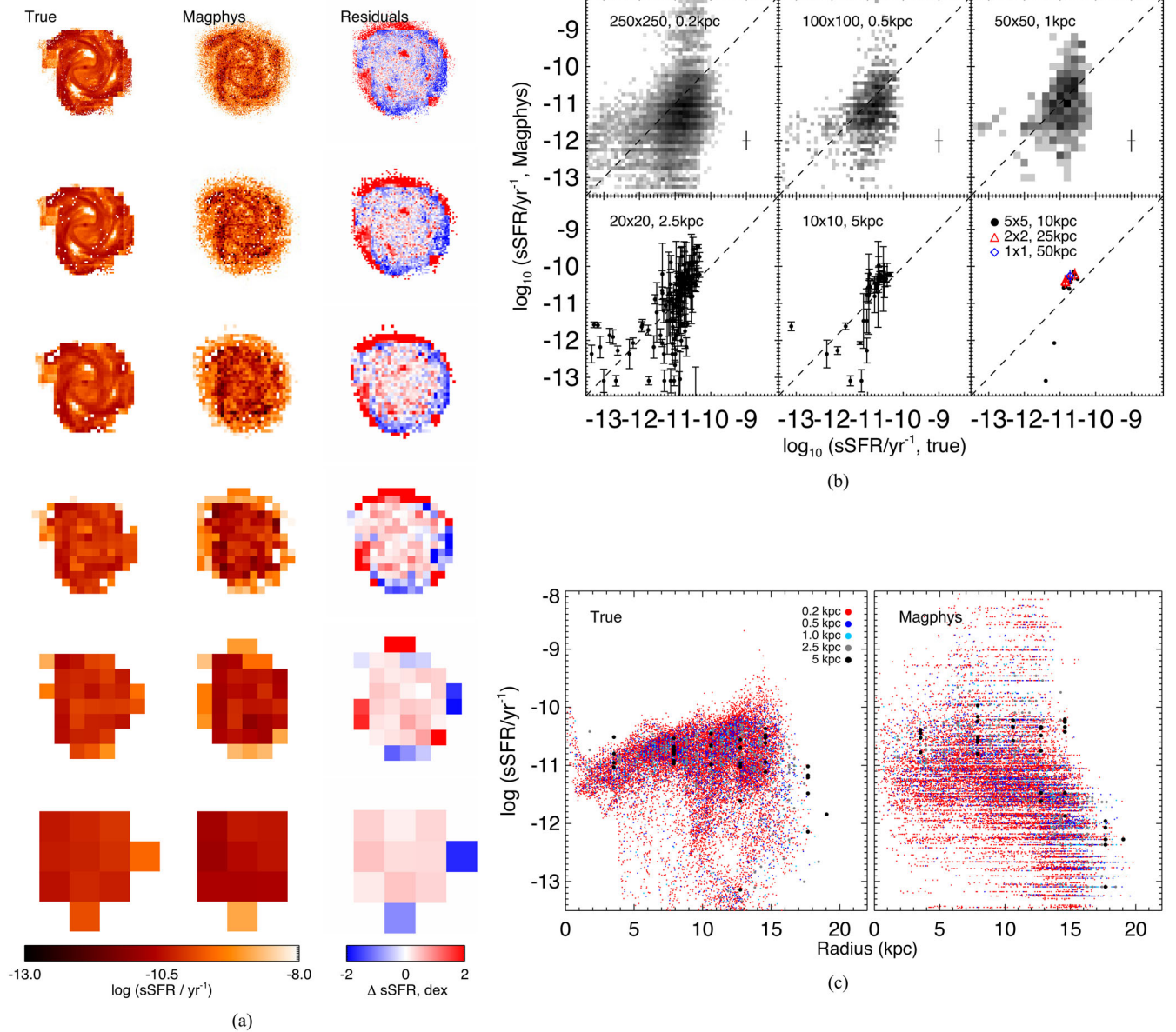quently, we multiply the dust masses output by MAGPHYS by 2 to account for this difference.

**Figure 9.** Recovery of sSFR for camera 0. The image colour scales for the images are as detailed in the bars underneath the corresponding columns, corresponding to $-13 < \log(\text{sSFR/yr}^{-1}) < -8$ and $-2 < \Delta\,\text{sSFR} < 2$ dex. For more details, see the caption of Fig. 4. For pixel sizes less than a few kpc, the scatter in the sSFR values recovered by MAGPHYS at fixed true sSFR is large. At lower resolutions, the sSFR is recovered reasonably well, although there is a systematic overestimate of the sSFR, which is caused by the overestimate of the SFR discussed above. The relatively flat sSFR profile is qualitatively recovered by MAGPHYS although there is larger scatter at fixed radius in the recovered values compared with the true ones.

age – for which modification of the default version of the code was required. Sections 3.7.1–3.7.3 represent exploratory tests, using the same methodology as the previous sections, of how well the MAGPHYS formalism can obtain reliable estimates of these parameters.

### 3.7.1 MAGPHYS recovery of stellar metallicity

Fig. 11(a) shows a comparison between metallicity maps taken from the simulations and those obtained from the MAGPHYS estimates. It is immediately clear that the MAGPHYS estimates (centre column) are noisier than the true values (left column). Although the general radial dependence is apparent in both the images and in Fig. 11(c), the recovered values at fixed radius exhibit larger scatter than the true approximately exponential profile, with the largest discrepancy in the central regions (see the right column of panel a).

Fig. 11(b) shows the relationship between the true and recovered metallicities for each of the different spatial resolutions; the MAGPHYS values are nearly always underestimates (reflected by the predominantly blue residual maps in Fig. 11 a), and they exhibit considerable scatter at fixed true metallicity. This is at odds with the results of Dye (2008, see Fig. 9 therein), who were able to recover the metallicity of a suite of mock composite stellar populations using only optical through near-infrared photometry. The discrepancy between our results is perhaps due to the far greater degree of realism in the current work (for example, the metallicity
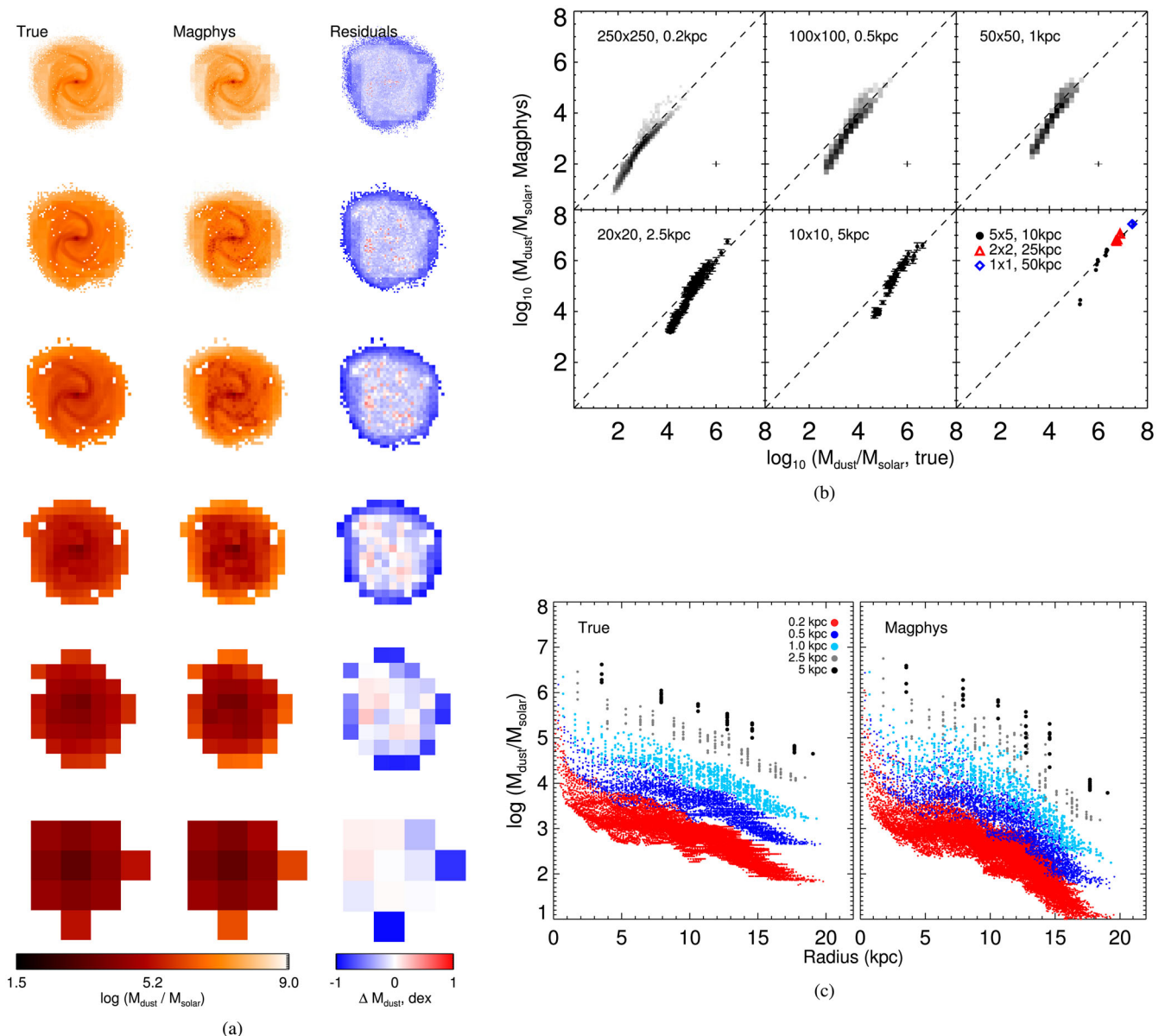
**Figure 10.** Recovery of dust mass for camera 0. The colour scales for the images showing the true and MAGPHYS -estimated mass distributions are given by the colour bars at the bottom of each column of panel (a). For more details, see the caption of Fig. 4. The details of the dust mass maps (e.g. spiral arms) are well recovered by MAGPHYS , as are the radial profiles. At all resolutions, the dust masses contained in individual pixels are recovered very well, except for the lowest dust mass pixels, for which the dust mass is systematically overestimated.

and degree of attenuation vary across the simulated disc employed in this work, and we employ full radiative transfer to produce the emergent SEDs). The difficulty in recovering metallicities using optical photometry alone is well demonstrated by Pacifici et al. (2012, their Fig. 11), who employed a suite of model galaxies from a semi-analytic model, which exhibit complex star formation histories, and Mentuch Cooper et al. (2012) further highlighted the difficulty of this task even using panchromatic data (albeit without energy balance). The MAGPHYS method of recovering metallicities is therefore potentially of great interest, since as mentioned in Section 1, the inclusion of far-infrared data can potentially break the well-known degeneracy between age and metallicity that affects photometry at optical/near-infrared wavelengths. However, this method is clearly not without its shortcomings, even though we are able to recover

the general trend of decreasing metallicity with increasing distance from the nucleus (but not the detailed radial profile). We intend to further investigate the ability of MAGPHYS to estimate metallicities from photometry using spectroscopic samples in a forthcoming investigation.

Fig. 5 shows the resolution dependence of the effective metallicity, calculated by summing the product of the metallicity and the stellar mass in each resolution element, and dividing the total by the total stellar mass (and propagating the uncertainties). The metallicity estimates show little evidence for variation as a function of resolution, with the values being broadly consistent within the error bars for the most face-on viewing angles. The one exception is the edge-on view, which is suggestive of a slight tendency to underestimate the metallicity in the unresolved case, though it is
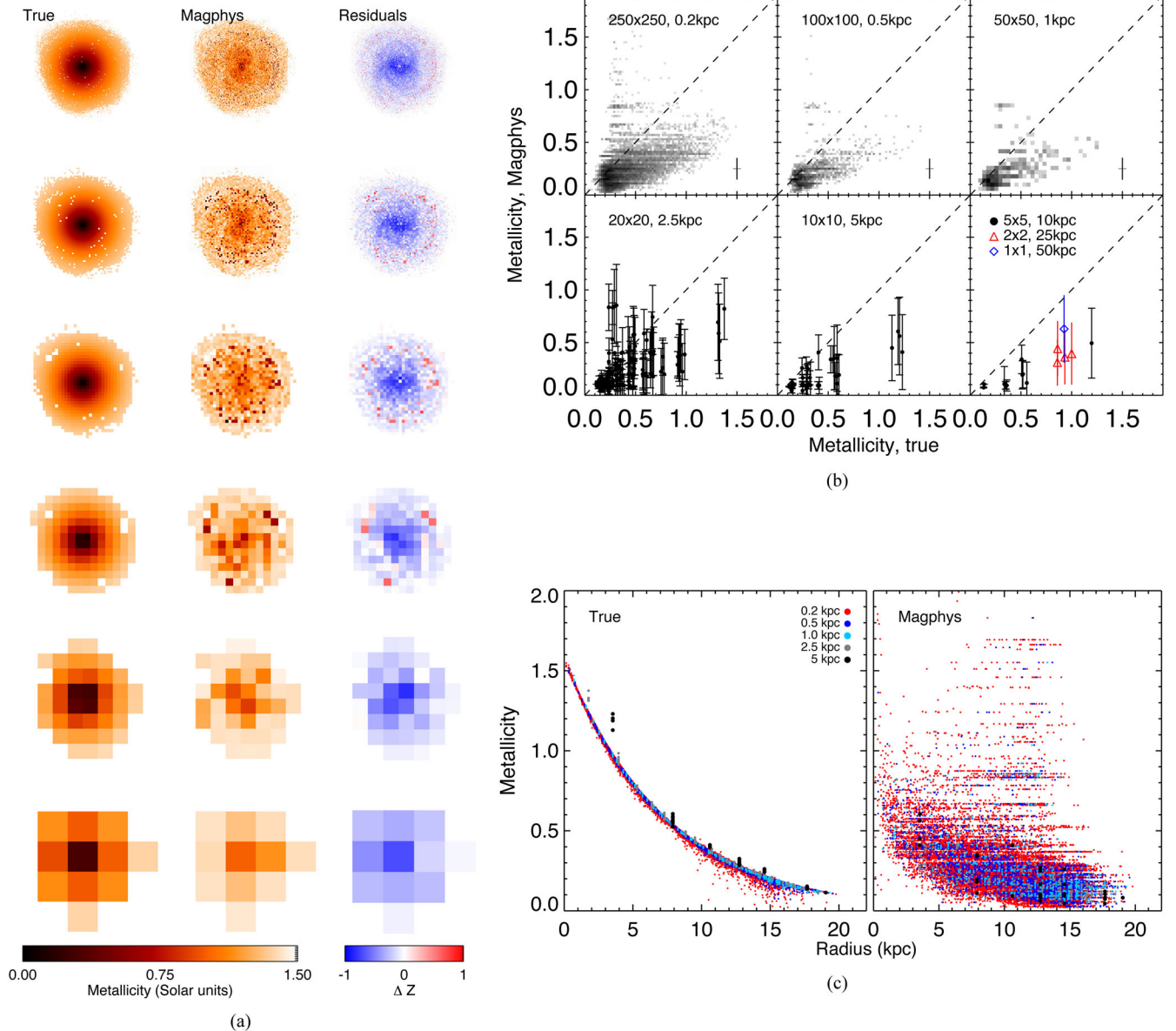
**Figure 11.** Recovery of metallicity for camera 0. The colour scales for each of the metallicity maps in panel (a) are given by the corresponding colour bars at the bottom of each column. For more details, see the caption of Fig. 4. The effective metallicity is systematically underestimated by MAGPHYS at all spatial resolutions, and there is considerable scatter in the recovered metallicity at fixed true metallicity (as also evident from the noisiness of the metallicity maps). Although MAGPHYS correctly infers that the metallicity decreases with radius, the detailed shape is not well recovered. Overall, these results demonstrate that recovering metallicity from even noiseless photometry that densely samples the UV through FIR is very challenging.

hard to find any conclusive evidence given the size of the error bars on the total values.

### 3.7.2 MAGPHYS recovery of V-band attenuation, $A_V$

In the three sub-plots of Fig. 12, we show the extent of our ability to estimate the visual extinction as a function of position across the disc. From examining Fig. 12, it is clear that MAGPHYS systematically overestimates the true $A_V$, however in many cases it is clear that this is because the true values are negative. This feature of the simulations comes about for two primary reasons. First, there is a physical effect (in both the simulations and in the real Universe): scattering of photons means that the emergent spectrum can sometimes

be brighter than the intrinsic spectrum at a given position (Wise & Silva 1996; Baes & Dejonghe 2002). Secondly, in low-surface brightness regions of the simulation, Monte Carlo noise can cause the emergent luminosity to be greater than the emitted luminosity (in the limit in which the luminosity is less than that carried by a single photon packet). Fig. 12(a) shows once more that MAGPHYS is able to broadly recover the trend of $A_V$ being largest in the nuclear region, and this feature is also visible in Fig. 12(c). While the high-resolution panels of Fig. 12(b) show that MAGPHYS is not especially effective at recovering low $A_V$, the situation is much improved at pixel sizes $\gtrsim$2.5 kpc, where we are able to obtain excellent $A_V$ estimates. At these lower resolutions, the scattering and small number Monte Carlo effects are much less noticeable since the individual
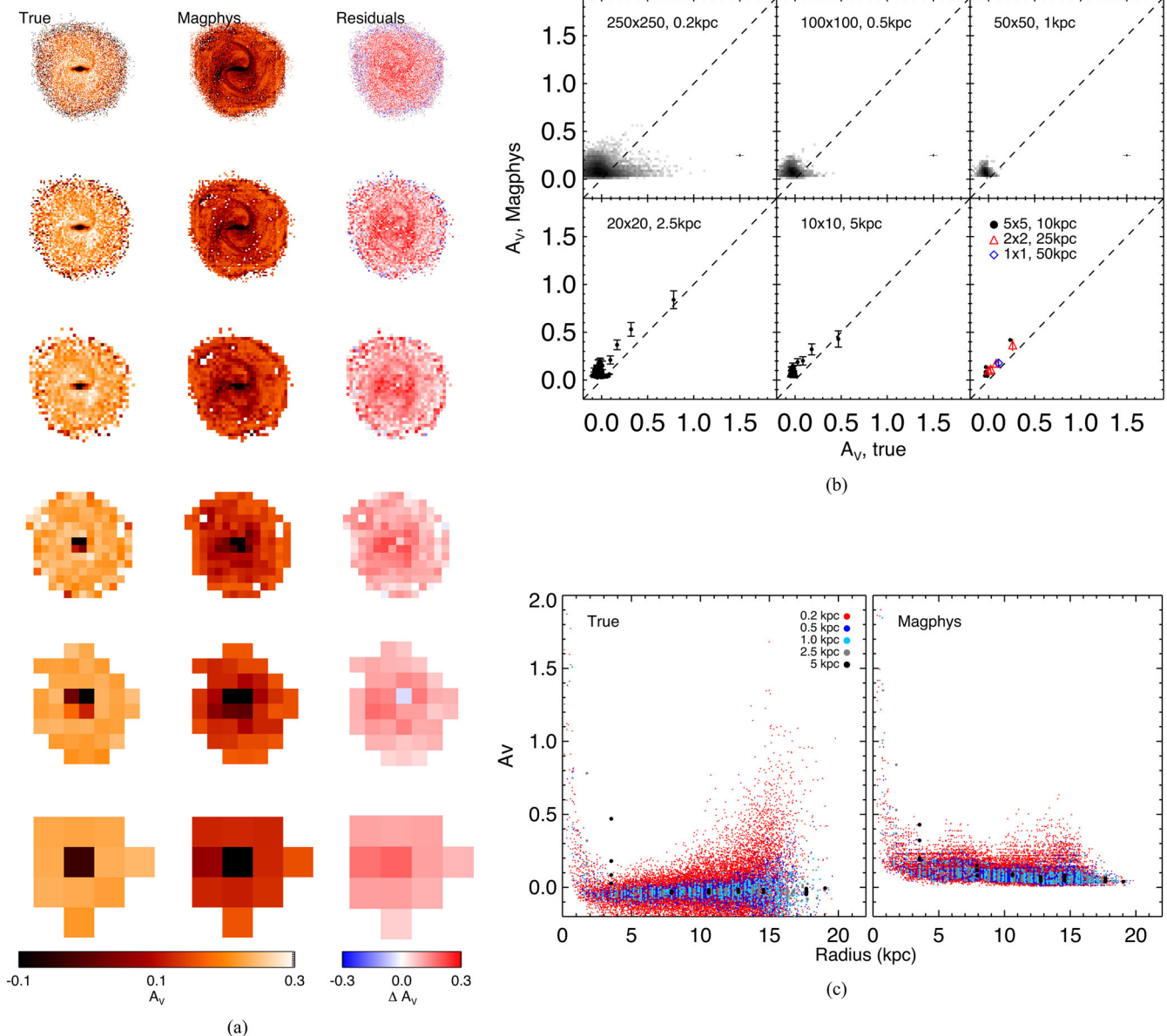
**Figure 12.** Recovery of $A_V$ for camera 0. As in previous figures, the colour bars showing the scale for each map of $A_V$ (true, MAGPHYS and difference, from left to right in panel a) are located at the bottom of the corresponding columns. For more details, see the caption of Fig. 4. The fact the $A_V$ is highest in the nucleus is recovered by MAGPHYS, but the contrast in $A_V$ between the spiral arms and inter-arm regions is overestimated. For pixel sizes greater than a few kpc, $A_V$ is reasonably well recovered, albeit slightly overestimated (by ∼0.1 mag). The negative $A_V$ values present in the simulations (which are due to scattered light and, in the low surface-brightess outskirts, can also be an artefact of Monte Carlo noise in the radiative transfer calculations), cannot be recovered by MAGPHYS owing to its assumed prior for $A_V$.

pixels contain more flux, and it is therefore not surprising that our $A_V$ estimates are much more effective in this regime. The aforementioned effects may also explain the erroneous appearance of enhanced spiral arm structure in the high-resolution images of $A_V$ values in Fig. 12(a). That the pixels with negative $A_V$ are comparatively faint (they all have less than 1 per cent of the peak $V$-band flux density), offers further support to our hypothesis.

We therefore conclude that MAGPHYS is reasonably effective at recovering trends in visual extinction within the simulated galaxies, albeit with a residual bias of up to 0.2 magnitudes, primarily dominated by regions with $A_V^{\text{true}} \lesssim 0$. It is, however, able to recover the increased obscuration in the nuclear region of this isolated disc galaxy irrespective of the spatial scales sampled.

### 3.7.3 MAGPHYS recovery of mass-weighted age, $Age_M$

Finally, we show the extent of our ability to recover the mass-weighted age using MAGPHYS in Fig. 13. The scatter in the MAGPHYS estimates is large at all spatial scales, though the situation is best for spatial pixels >10 kpc in size, where the average age underestimate is around 0.3 dex, slightly larger than the MAGPHYS error bars. While the radial dependence of the true stellar population age occupies a tight locus in the left-hand panel of Fig. 13(c), the same can not be said of the MAGPHYS estimates, for which the scatter is also around 0.2–0.3 dex. Perhaps the best way to describe the MAGPHYS estimates of mass-weighted age is that they are of limited use since the offset scatter is so large, however it will be of particular
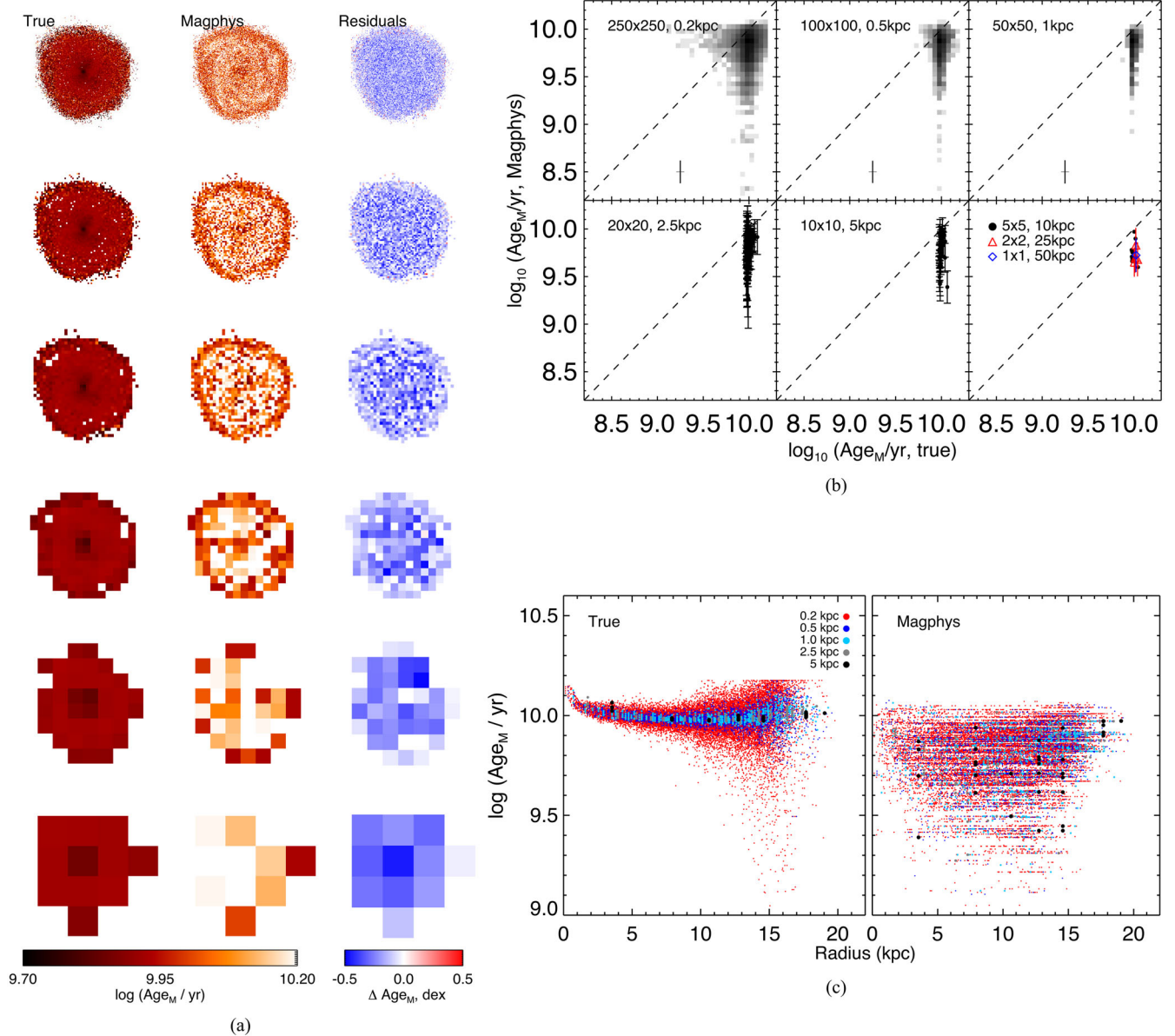
**Figure 13.** Recovery of mass-weighted age for camera 0. For more details, see the caption of Fig. 4. MAGPHYS tends to underestimate the mass-weighted age, likely because the bulk of the pixels are dominated by ∼10 Gyr-old stellar populations, and integrated photometry does not depend strongly on age for stellar populations with ages ≫1 Gyr.

interest to see whether this trend persists for a larger sample of simulated galaxies.

# 4 DISCUSSION

## 4.1 Acceptable fits

In this work, we have performed a controlled experiment on the efficacy of MAGPHYS for recovering the spatially resolved properties of galaxies, a task for which it was not designed. MAGPHYS is able to recover statistically acceptable fits to >99 per cent of the pixels enclosed within the *r*-band effective radius of the simulated galaxy, and between 61 and 77 per cent of the pixels within the region emitting 99 per cent of the total *r*-band light (at 200 pc and 5 kpc resolution, respectively). With MAGPHYS , we are able to produce a

larger fraction of acceptable fits out to larger radii at lower spatial resolution, consistent with larger regions being better approximated by the simple galaxy model used by MAGPHYS . These results are in general agreement with the MAGPHYS study of M31 by Viaene et al. (2014), however since we are basing our study on a simulation, we are also able to determine whether or not the parameters that MAGPHYS derives are reasonable, and we will discuss this in the coming sub-sections.

## 4.2 The influence of spatial resolution on integrated parameters

As well as producing statistically acceptable fits, we are able to recover realistic integrated galaxy properties, that in general show little strong evidence for dependence on spatial resolution once

the uncertainties on the individual parameter estimates (e.g. the MAGPHYS stellar mass estimates in each pixel) are taken into account. MAGPHYS produces the best integrated parameter estimates on the almost edge-on simulation, consistent with the idea that along these sightlines we are observing through a larger volume of the galaxy, for which the assumed energy balance criterion is more reasonable than e.g. for the face-on case (in which the photometry comes from integrating through a geometrically thin disc).

The lack of resolution dependence in the stellar mass estimation is apparently at odds with Sorba & Sawicki (2015), who found that spatially resolved photometry underestimates the true mass of galaxies, especially those with higher specific star formation rates. While our best-fitting stellar mass estimates are smaller than the sum of the resolved values, they are consistent with each other within the uncertainties. In addition, since our simulation-based approach enables us to know the true stellar mass, we are able to see that it is the high-resolution stellar mass estimate which is biased relative to the truth, by ∼0.05–0.07 dex. Furthermore, according to the Sorba & Sawicki (2015) relation for the bias in stellar mass estimates, the size of the expected bias at the true specific SFR of the galaxy snapshot used in this work ($\log_{10}$ sSFR $\approx -10.72$ yr$^{-1}$) is a factor of 0.95 for this comparatively quiescent source. This factor is smaller than the uncertainties associated with our (and indeed, *all*) stellar mass estimates; it is possible therefore that the trend they report will be clearer if we were to study more actively star-forming galaxy simulations (which are predicted to have larger biases according to the Sorba & Sawicki 2015 formula). Sorba & Sawicki (2015) also suggested a sharp decrease in the pixel-by-pixel stellar mass estimates at a physical scale of 3 kpc, for which we see no evidence in this study.

While the integrated stellar mass estimates show little evidence for resolution bias, there is more evidence in other parameters. With SFR (and sSFR) and dust mass, this is primarily due to the sub-kpc-resolution data cubes, which are of course those for which the MAGPHYS model is least appropriate. The lower-resolution data cubes with ≳ kpc scale pixels show little or no evidence for resolution-dependent bias. Interestingly, the effective metallicity does not exhibit a resolution bias for any of the three viewing angles to the simulated galaxy, but the recovery is poor, in general. These potential resolution-dependent biases may be of particular concern if they still hold after we have considered a larger suite of simulations that span a wider range of galaxy properties.

### 4.3 Radial dependence and variation across the projected disc

MAGPHYS produces reasonable results when we attempt to recover the radial and projected distributions of stellar mass, dust luminosity, SFR, sSFR, dust mass, and $A_V$, especially when the pixel scale is ≳1 kpc. The stellar, dust luminosity and dust mass estimates are sufficiently accurate that we can clearly discern spiral structure even in the radial distributions of the recovered parameters, including stellar masses as low as $10^4$ M$_\odot$ and dust luminosities and masses as low as $10^3$ L$_\odot$/$10 - 100$ M$_\odot$.

Our results for sSFR highlight the difficulties associated with estimating values for individual pixels; the derived sSFRs are highly uncertain, and even with model panchromatic photometry, and in the absence of resolution effects, it is difficult to recover any real radial dependence. Though there is little evidence for overall bias in the sSFR estimates, there is considerable scatter, especially in the higher resolution simulations for lower surface-brightness pixels. These results should therefore serve as a note of caution for works attempting to detect decreased sSFR near the centres of galaxies, as

evidence of an 'inside-out' quenching mechanism in galaxies based on photometry alone (e.g. Viaene et al. 2014; Jung et al. 2017, at low- and high-redshift, respectively), and similar issues could arise if sSFRs are simply estimated from photometry without fitting SEDs (as in Tacchella et al. 2015, 2017, for example). At the same time, it is possible that these uncertainties on sSFR may be reduced by making some assumptions about the prior distribution of e.g. stellar mass, rather than fitting individual pixels independently, and as we have noted, the sSFR estimates are far better when averaging over larger regions. Our MAGPHYS results also reveal an anomalous annular region of low-sSFR pixels at the edge of the disc; this region is not present in the real data, and a similar effect is reported in the outermost ring of M31 in the MAGPHYS study by Viaene et al. (2014).

Among the non-standard outputs that we have extracted from MAGPHYS by making simple modifications to the code and using the standard libraries, we found that MAGPHYS is effective for making reliable estimates of $A_V$ for pixel sizes ≳2.5 kpc,. Although the radial trend in metallicity is qualitatively recovered, the quantitative success of the recovery is more limited for metallicity than for the other properties considered. The mass-weighted age is not well recovered in detail, likely because the bulk of the pixels are dominated by ∼10 Gyr-old stellar populations, and integrated photometry does not depend strongly on age for stellar populations with ages ≫1 Gyr. That MAGPHYS is able to at least qualitatively recover the metallicity gradient in the simulated galaxy is particularly interesting, despite the bias towards lower values and scatter of around $\delta Z \approx 0.2$ in the recovered values. With Amblard et al. (2017), for example, finding evidence for radial dependence in the metallicity of NGC 2768 and IC 1459, albeit using the CIGALEMC code from (Serra et al. 2011, which also has an energy balance criterion at its core), further validation of the ability of energy balance codes to estimate metallicities from photometry is essential. Forthcoming observations with new and forthcoming arcminute-scale integral field spectrographs, as well as comparing integrated photometry with already existing spectroscopic data sets, will be ideal for these purposes.

### 4.4 Limitations

In this work, we have studied 'only' a single simulated isolated disc galaxy, observed at a single snapshot in time and assuming a constant signal-to-noise ratio in 21 different bands of photometry, with just three different viewing angles. Moreover, the simulation was designed to be representative (in terms of e.g. gas fraction) of galaxies of similar mass in the local Universe, and its dust obscuration is modest. Thus, our conclusions may not be generalizable to higher-redshift or/and more highly dust-obscured galaxies.

Still, to perform this simple test, we produced a total 75 530 different SED fits for each camera angle (i.e. 226 590 SED fits in total), requiring around $3 \times 10^4$ CPU hours just for the MAGPHYS SED fitting. This work therefore represents a very encouraging first look at the issue of how well energy-balance SED fitting can be applied to spatially resolved photometry. It will be of particular interest to study how well this technique works for a range of different simulations, spanning a range of different redshifts, in different stages of activity, with widely varying levels of dust content, and with different photometric coverage, alongside comparisons with new and forthcoming spectroscopic data sets to provide important additional cross-examination. We intend to build on our growing body of work in this area to lead the effort required to tackle these important questions.

## 5 CONCLUSIONS

We have performed a numerical experiment, in which we have used a simulation of an isolated disc galaxy to test the ability of the widely used energy balance spectral energy distribution (SED) fitting code MAGPHYS (da Cunha et al. 2008) to estimate physical parameters of spatially resolved observations of galaxies. We used MAGPHYS to fit more than 250 000 individual pixels ranging from 10 to 0.2 kpc in size, at three different viewing angles towards the simulated galaxy at a single time snapshot, using 21 bands of multiwavelength photometry spanning the ultraviolet to the far-infrared. We have used the default version of MAGPHYS , making only trivial modifications similar to those in our previous work (Smith & Hayward 2015, which focused on photometric constraints on galaxy star formation histories) to allow us to produce estimates of mass-weighted age, metallicity and visual extinction ($A_V$). This task is done in post-processing, and allows us to produce marginalized probability distributions for each parameter, derived using the energy balance criterion.

MAGPHYS is able to produce statistically acceptable fits to >99 per cent of the pixels within the *r*-band effective radius, and between 59 and 77 per cent of the pixels within a 20 kpc radius (where 99 per cent of the total *r*-band luminosity is emitted). This is true despite being based on an energy balance criterion, which must break down on at small scales (i.e. when the dust emission from a given pixel is not predominately powered by stellar emission from within the same pixel) and being supplied with libraries of stellar populations and dust emission that are built with whole galaxies in mind. As well as producing acceptable fits, we use the known true values from the simulations to compare the derived values of stellar mass, dust luminosity, SFR, sSFR, stellar metallicity, $A_V$, dust mass, and mass-weighted age. We find that MAGPHYS produces reasonable parameter estimates for stellar mass, dust luminosity, SFR, sSFR, $A_V$, and dust mass in these challenging situations for which it was not intended; the recovery of stellar metallicity and mass-weighted age (which are not standard MAGPHYS outputs) is less effective.

While we are unable to reproduce claims in the literature for resolution-dependent bias in stellar mass estimates based on SED fitting, we see tentative evidence for resolution-dependent biases in the SFR, sSFR, and dust mass estimates. We intend to investigate this concerning issue more in more detail, using a larger suite of simulations, in a forthcoming work. Despite this, the overall offsets that we see on integrated parameters (produced by summation of the values for individual pixels) are generally consistent with those derived based on the integrated photometry in our previous study (Hayward & Smith 2015).

As well as the integrated parameters, we find that MAGPHYS does a generally good job of recovering the radial and projected variation in all of the aforementioned parameters, at least qualitatively, with the possible exception of specific star formation rate, which is difficult to interpret in the highest resolution simulations, primarily in the inter-arm and outermost regions of the stellar disc simulation (although the uncertainties are large). This may be due to the influence of the energy balance criterion, which does not apply in pixels in which the majority of photons heating the dust originate from nearby regions rather than being emitted by stars within the pixel. These results highlight the need for extreme caution when using photometry to search for evidence of e.g. inside out quenching, indicated by possible radial variation in estimates of sSFR (e.g. Viaene et al. 2014; Jung et al. 2017).

As mentioned above, we intend to expand on this work in a future publication by analysing a suite of simulated galaxies that span a broader range of galaxy properties. We also intend to further test the efficacy of using MAGPHYS to estimate metallicities based on photometry alone, using samples of real galaxies for which panchromatic photometry and spectroscopic metallicity estimates are available.

## REFERENCES

Acquaviva V., 2016, MNRAS, 456, 1618
Amblard A., Temi P., Gaspari M., Brighenti F., 2017, ApJ, 834, 20
Aniano G. et al., 2012, ApJ, 756, 138
Bacon R. et al., 2010, in McLean I. S., Ramsay S. K., Takami H., eds, Proc. SPIE Conf. Ser. Vol. 7735, Ground-based and Airborne Instrumentation for Astronomy III. SPIE, Bellingham, p. 773508
Baes M., Dejonghe H., 2002, MNRAS, 335, 441
Baes M. et al., 2010, A&A, 518, L39
Berta S. et al., 2013, A&A, 551, A100
Bruzual G., Charlot S., 2003, MNRAS, 344, 1000
Bundy K. et al., 2015, ApJ, 798, 7
Burgarella D., Buat V., Iglesias-Páramo J., 2005, MNRAS, 360, 1413
Carter D. et al., 2009, MNRAS, 397, 695
Chabrier G., 2003, PASP, 115, 763
Charlot S., Fall S. M., 2000, ApJ, 539, 718
Cibinel A. et al., 2015, ApJ, 805, 181
Cox T. J., Jonsson P., Somerville R. S., Primack J. R., Dekel A., 2008, MNRAS, 384, 386
da Cunha E., Charlot S., Elbaz D., 2008, MNRAS, 388, 1595
da Cunha E., Charmandaris V., Díaz-Santos T., Armus L., Marshall J. A., Elbaz D., 2010, A&A, 523, A78
Dalton G. et al., 2012, in McLean I. S., Ramsay S. K., Takami H., eds, Proc. SPIE Conf. Ser. Vol. 8446, Ground-based and Airborne Instrumentation for Astronomy IV. SPIE, Bellingham, p. 84460P
Dalton G. et al., 2014, in McLean I. S., Ramsay S. K., Takami H., eds, Proc. SPIE Conf. Ser. Vol. 9147, Ground-based and Airborne Instrumentation for Astronomy V. SPIE, Bellingham, p. 91470L
Dariush A. et al., 2016, MNRAS, 456, 2221
De Looze I., Baes M., Fritz J., Verstappen J., 2012, MNRAS, 419, 895
De Looze I. et al., 2014, A&A, 571, A69
Dole H. et al., 2006, A&A, 451, 417
Draine B. T., Li A., 2007, ApJ, 657, 810
Dunlop J. S. et al., 2017, MNRAS, 466, 861
Dunne L., Eales S., Edmunds M., Ivison R., Alexander P., Clements D. L., 2000, MNRAS, 315, 115
Dwek E., 1998, ApJ, 501, 643
Dye S., 2008, MNRAS, 389, 1293
Dye S. et al., 2015, MNRAS, 452, 2258
Fazio G. G. et al., 2004, ApJS, 154, 10
Galliano F. et al., 2011, A&A, 536, A88
Giovannoli E., Buat V., Noll S., Burgarella D., Magnelli B., 2011, A&A, 525, A150

Griffin M. J. et al., 2010, A&A, 518, L3

Groves B., Dopita M. A., Sutherland R. S., Kewley L. J., Fischera J., Leitherer C., Brandl B., van Breugel W., 2008, ApJS, 176, 438

Groves B. et al., 2012, MNRAS, 426, 892

Gurkan G. et al., 2018, MNRAS, 475, 3010

Hardcastle M. J. et al., 2016, MNRAS, 462, 1910

Hartley W. G. et al., 2013, MNRAS, 431, 3045

Hayward C. C., Smith D. J. B., 2015, MNRAS, 446, 1512

Hayward C. C., Kereš D., Jonsson P., Narayanan D., Cox T. J., Hernquist L., 2011, ApJ, 743, 159

Hayward C. C., Jonsson P., Kereš D., Magnelli B., Hernquist L., Cox T. J., 2012, MNRAS, 424, 951

Hayward C. C., Torrey P., Springel V., Hernquist L., Vogelsberger M., 2014a, MNRAS, 442, 1992

Hayward C. C. et al., 2014b, MNRAS, 445, 1598

Hopkins P. F., Richards G. T., Hernquist L., 2007, ApJ, 654, 731

Hurley P. D. et al., 2017, MNRAS, 464, 885

Illingworth G. D. et al., 2013, ApJS, 209, 6

James A., Dunne L., Eales S., Edmunds M. G., 2002, MNRAS, 335, 753

Jarvis M. J. et al., 2013, MNRAS, 428, 1281

Johnston R., Vaccari M., Jarvis M., Smith M., Giovannoli E., Häußler B., Prescott M., 2015, MNRAS, 453, 2540

Johnston E. J. et al., 2017, MNRAS, 465, 2317

Jonsson P., 2006, MNRAS, 372, 2

Jonsson P., Groves B. A., Cox T. J., 2010, MNRAS, 403, 17

Jung I. et al., 2017, ApJ, 834, 81

Kennedy R. et al., 2016, MNRAS, 460, 3458

Kennicutt R. C., Jr, 1998, ApJ, 498, 541

Kennicutt R. C. et al., 2011, PASP, 123, 1347

Kroupa P., 2001, MNRAS, 322, 231

Lanz L. et al., 2013, ApJ, 768, 90

Lanz L., Hayward C. C., Zezas A., Smith H. A., Ashby M. L. N., Brassington N., Fazio G. G., Hernquist L., 2014, ApJ, 785, 39

Lawrence A. et al., 2007, MNRAS, 379, 1599

Lee H.-c., Worthey G., Trager S. C., Faber S. M., 2007, ApJ, 664, 215

Leitherer C. et al., 1999, ApJS, 123, 3

Martin D. C. et al., 2005, ApJ, 619, L1

Mentuch Cooper E. et al., 2012, ApJ, 755, 165

Merlin E. et al., 2015, A&A, 582, A15

Michałowski M. J., Hayward C. C., Dunlop J. S., Bruce V. A., Cirasuolo M., Cullen F., Hernquist L., 2014, A&A, 571, A75

Miettinen O. et al., 2017, A&A, 597, A5

Noll S., Burgarella D., Giovannoli E., Buat V., Marcillac D., Muñoz-Mateos J. C., 2009, A&A, 507, 1793

Pacifici C., Charlot S., Blaizot J., Brinchmann J., 2012, MNRAS, 421, 2002

Pearson W. J., Wang L., van der Tak F. F. S., Hurley P. D., Burgarella D., Oliver S. J., 2017, A&A, 603, 8

Pilbratt G. L. et al., 2010, A&A, 518, L1

Poggianti B. M. et al., 2001, ApJ, 562, 689

Poglitsch A. et al., 2010, A&A, 518, L2

Reddy N. A., Steidel C. C., Pettini M., Bogosavljević M., Shapley A. E., 2016, ApJ, 828, 108

Rieke G. H. et al., 2004, ApJS, 154, 25

Roebuck E., Sajina A., Hayward C. C., Pope A., Kirkpatrick A., Hernquist L., Yan L., 2016, ApJ, 833, 60

Rowlands K. et al., 2014a, MNRAS, 441, 1017

Rowlands K., Gomez H. L., Dunne L., Aragón-Salamanca A., Dye S., Maddox S., da Cunha E., van der Werf P., 2014b, MNRAS, 441, 1040

Safarzadeh M., Hayward C. C., Ferguson H. C., 2017, ApJ, 840, 15

Sanders N. E., Levesque E. M., Soderberg A. M., 2013, ApJ, 775, 125

Schmidt M., 1959, ApJ, 129, 243

Serra P., Amblard A., Temi P., Burgarella D., Giovannoli E., Buat V., Noll S., Im S., 2011, ApJ, 740, 22

Smail I., Kuntschner H., Kodama T., Smith G. P., Packham C., Fruchter A. S., Hook R. N., 2001, MNRAS, 323, 839

Smith D. J. B., Hayward C. C., 2015, MNRAS, 453, 1597

Smith D. J. B. et al., 2012, MNRAS, 427, 703

Smith D. J. B. et al., 2013, MNRAS, 436, 2435

Snyder G. F., Cox T. J., Hayward C. C., Hernquist L., Jonsson P., 2011, ApJ, 741, 77

Snyder G. F., Hayward C. C., Sajina A., Jonsson P., Cox T. J., Hernquist L., Hopkins P. F., Yan L., 2013, ApJ, 768, 168

Sorba R., Sawicki M., 2015, MNRAS, 452, 235

Springel V., 2005, MNRAS, 364, 1105

Springel V., 2010, MNRAS, 401, 791

Springel V., Hernquist L., 2003, MNRAS, 339, 289

Springel V. et al., 2005, Nature, 435, 629

Swinbank A. M. et al., 2015, ApJ, 806, L17

Tacchella S. et al., 2015, Science, 348, 314

Tacchella S. et al., 2017, ApJ, preprint (arXiv:1704.00733)

Tanaka M. et al., 2017, preprint (arXiv:1706.00566)

Viaene S. et al., 2014, A&A, 567, A71

Viaene S. et al., 2016, A&A, 586, A13

Viero M. P. et al., 2013, ApJ, 779, 32

Vika M., Bamford S. P., Häußler B., Rojas A. L., 2014, MNRAS, 444, 3603

Werner M. W. et al., 2004, ApJS, 154, 1

Wise M. W., Silva D. R., 1996, ApJ, 461, 155

Worthey G., 1994, ApJS, 95, 107

Wright A. H. et al., 2016, MNRAS, 460, 765

Wuyts S., Cox T. J., Hayward C. C., Franx M., Hernquist L., Hopkins P. F., Jonsson P., van Dokkum P. G., 2010, ApJ, 722, 1666

Wylezalek D., Zakamska N. L., Liu G., Obied G., 2016, MNRAS, 457, 745

York D. G. et al., 2000, AJ, 120, 1579

Younger J. D., Hayward C. C., Narayanan D., Cox T. J., Hernquist L., Jonsson P., 2009, MNRAS, 396, L66

## APPENDIX A: ADDITIONAL FIGURES

Here, we include figures showing comparisons of projected maps of (a) stellar mass, (b) dust luminosity, (c) SFR, (d) sSFR, (e) dust-mass, (f) metallicity, (g) $A_V$, and (h) mass-weighted age for the different viewing angles, with camera 3 shown in Fig. A1 and camera 5 in Fig. A2.
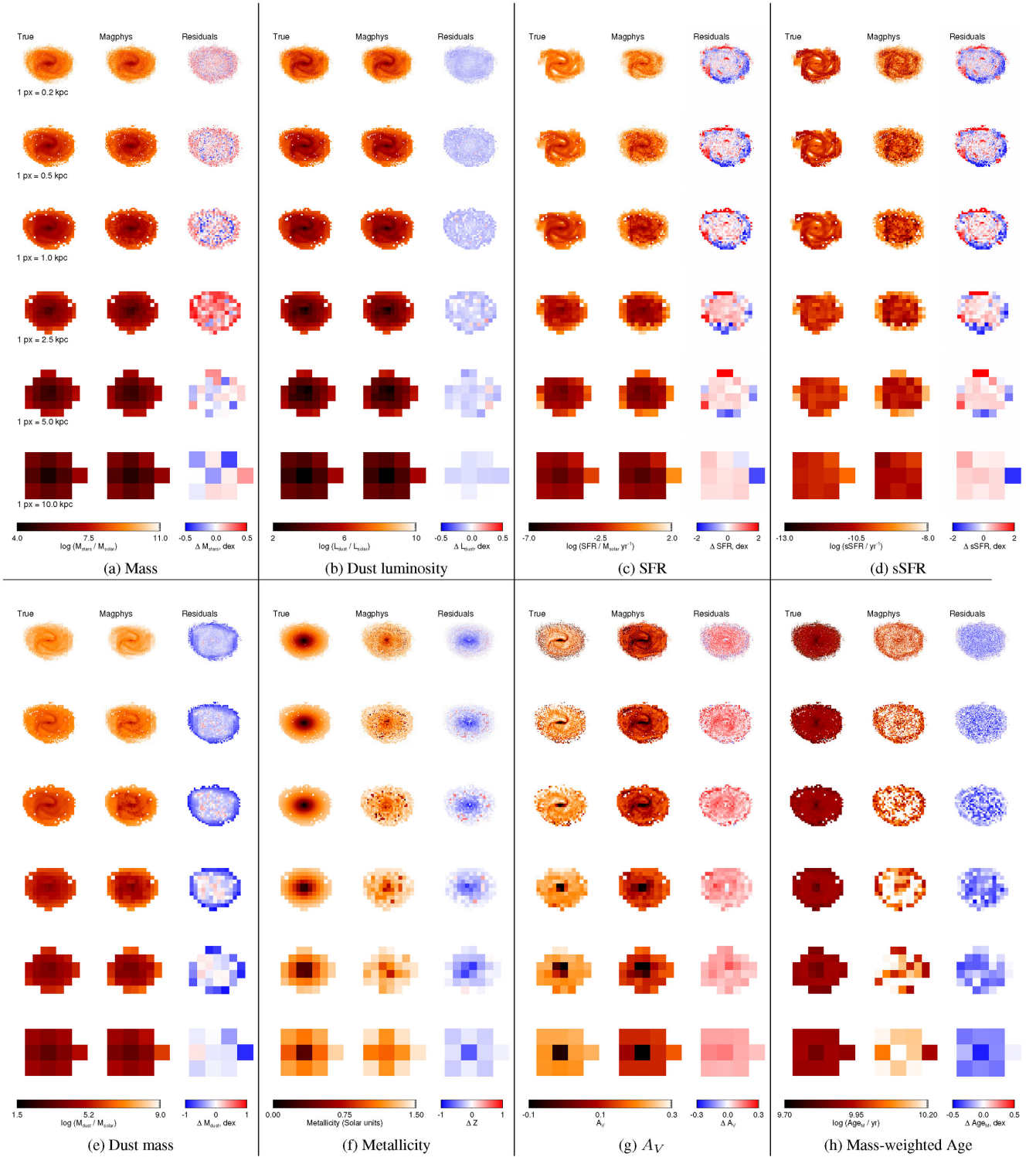
**Figure A1.** Each sub-panel shows comparisons between the true (left) and MAGPHYS -derived values of (a) stellar mass, (b) dust luminosity, (c) SFR, (d) specific-SFR, (e) dust mass, (f) Metallicity, (g) $A_V$, and (h) mass-weighted age for our simulated galaxy snapshot viewed from camera 3, at a range of spatial resolutions from 0.2 kpc pixels (top) to 10 kpc pixels (bottom).
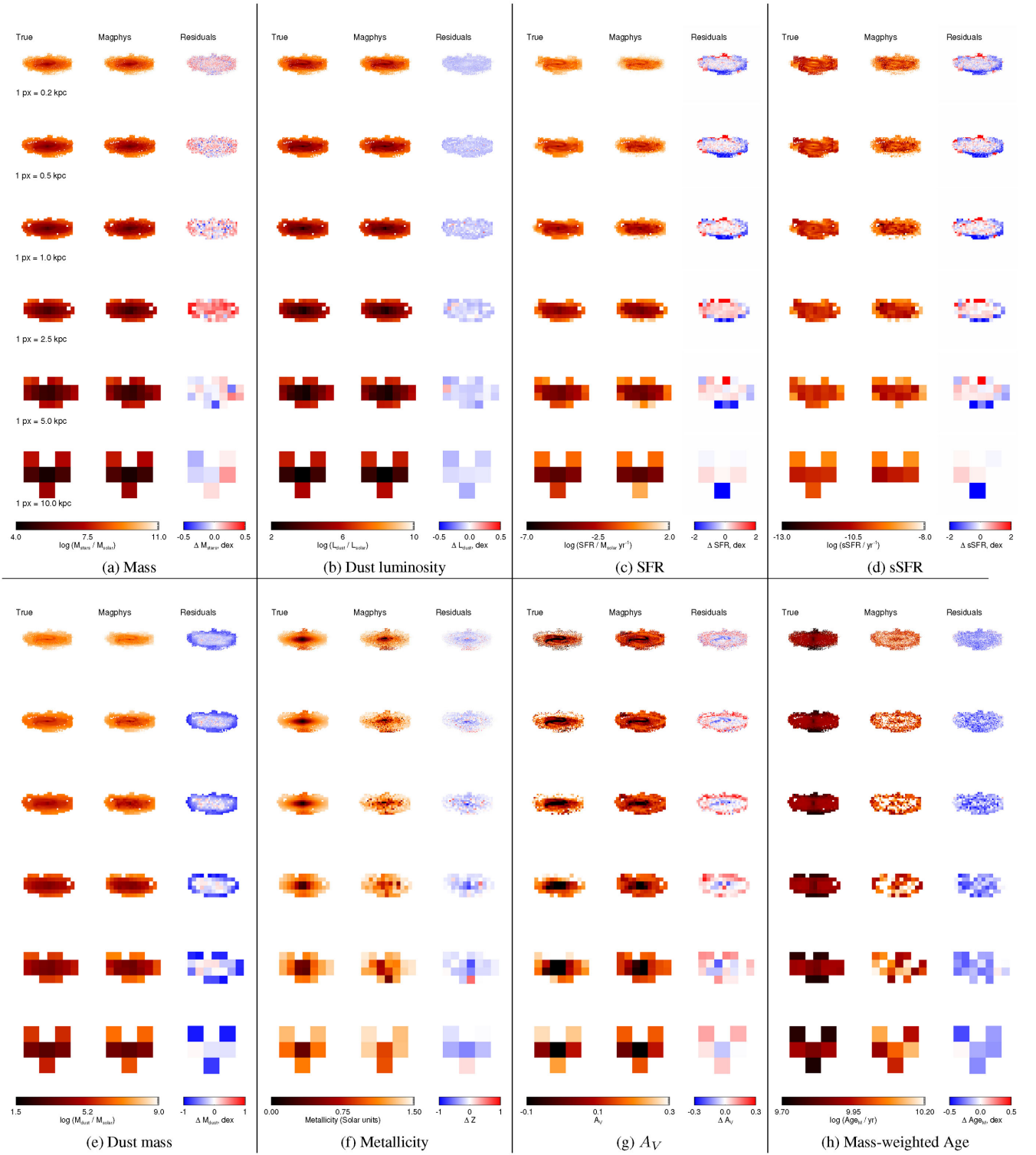
**Figure A2.** Similar to Fig. A2, but for camera 5 (the nearly edge-on view).

This paper has been typeset from a TEX/LATEX file prepared by the author.